

PHYSICS **OF THE** SOLAR CORONA

An Introduction with Problems and Solutions

MARKUS
ASCHWANDEN

 Springer

PRAXIS 

Chapter 1

Introduction

1.1 History of Solar Corona Observations

What we see with our eye from our Sun or from the billions of stars in our galaxy is optical radiation that is emitted at the surface of the star, in the so-called photosphere. The optical emission produced by Thomson scattering in the much more tenuous atmosphere or corona above, is many orders of magnitude less intense and thus can only be seen when the solar surface is occulted (e.g., by the moon during a total solar eclipse). The first observations of the solar corona thus date back to ancient eclipse observations, which have been reported from Indian, Babylonian, or Chinese sources. A detailed account of historical eclipses can be found in the book of Guilmier & Koutchmy (1999), which mentions, for example Chinese solar eclipses as early as 2800 BC, the failure of a prediction by the two luckless Chinese royal astrologers Hsi and Ho around 2000 BC, the successful prediction of the solar eclipse of 28 May 585 BC by the Greek mathematician and philosopher Thales, or the eclipse of 1919 May 29 in Sobral (Brazil) and Principe (West Africa), which has been observed by two expeditions of the British astronomer Arthur Stanley Eddington to prove Einsteins theory of relativity.

Regular observations of solar eclipses and prominences started with the eclipse of 1842, which was observed by experienced astronomers like Airy, Arago, Baily, Littrow, and Struve. Photographic records start since the 1851 eclipse in Norway and Sweden, when the professional photographer Berkowski succeeded to produce a daguerrotype of prominences and the inner corona. Visual and spectroscopic observations of prominence loops were carried out by Pietro Angelo Secchi in Italy and by Charles Augustus Young of Princeton University during the 19th century. The element helium was discovered in the solar corona by Jules Janssen in 1868. George Ellery Hale constructed a spectroheliograph in 1892 and observed coronal lines during eclipses. Bernard Lyot built his first coronagraph at the Pic-du-Midi Observatory in 1930, an instrument that occults the bright solar disk and thus allows for routine coronal observations, without need to wait for one of the rare total eclipse events. In 1942, Edlén identified forbidden lines of highly ionized atoms and in this way established for the first time the

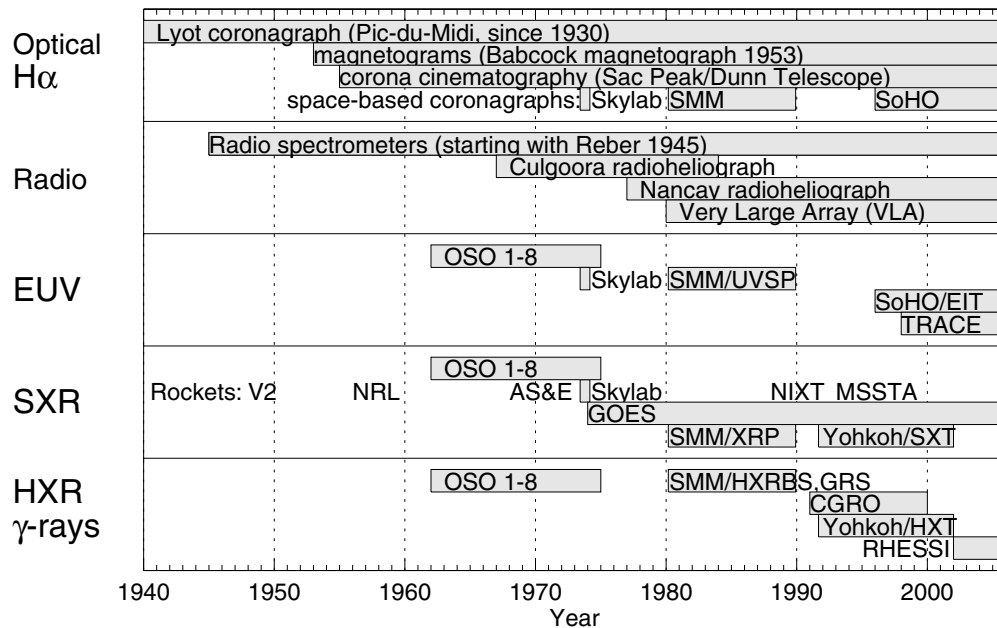


Figure 1.1: The operation periods of major instruments and space missions that provided unique observations of the solar corona are shown in historical order, sorted in different wavelength regimes.

million-degree temperature of the corona. A historical chronology of these early coronal observations is given in Bray et al. (1991), while coronal observations in the space age are reviewed in the encyclopedia article of Alexander & Acton (2002).

If we observe the Sun or the stars in other wavelengths, for instance in soft X-rays, hard X-rays, or radio wavelengths, the brightest emission comes from the corona, while the photosphere becomes invisible, just opposite to optical wavelengths. A breakthrough of coronal observations therefore started with the space era of rocket flights and spacecraft missions, which enabled soft X-ray and extreme ultraviolet (EUV) observations above the absorbing Earth's atmosphere (Fig. 1.1). Early Areobee rocket flights were conducted by the U.S. *Naval Research Laboratory (NRL)* in 1946 and 1952, recording spectrograms at EUV wavelengths down to 190 nm and Lyman- α emission of H I at 121.6 nm. In 1974, G. Brueckner and J.D. Bartoe achieved a resolution of $\approx 4''$ in EUV lines of He I, He II, O IV, O V, and Ne VII. The first crude X-ray photograph of the Sun was obtained by Friedman in 1963 with a pinhole camera from an Areobee rocket of *NRL* on 1960 April 19. These rocket flights last typically about 7 minutes, and thus allow only for short glimpses of coronal observations. Long-term observations were facilitated with the satellite series *Orbiting Solar Observatory (OSO-1 to OSO-8)*, which were launched into orbit during 1962–1975, equipped with non-imaging EUV, soft X-ray, and hard X-ray spectrometers and spectroheliographs. Finally, the launch of *Skylab*, which operated from 1973 May 14 to 1974 February 8 initiated a new era of multi-wavelength solar observations from space. *Skylab* carried a white-light coronagraph, two grazing-incidence X-ray telescopes, EUV spectroheliometers/spectroheliographs, and an UV spectrograph, recording $\approx 32,000$ pho-

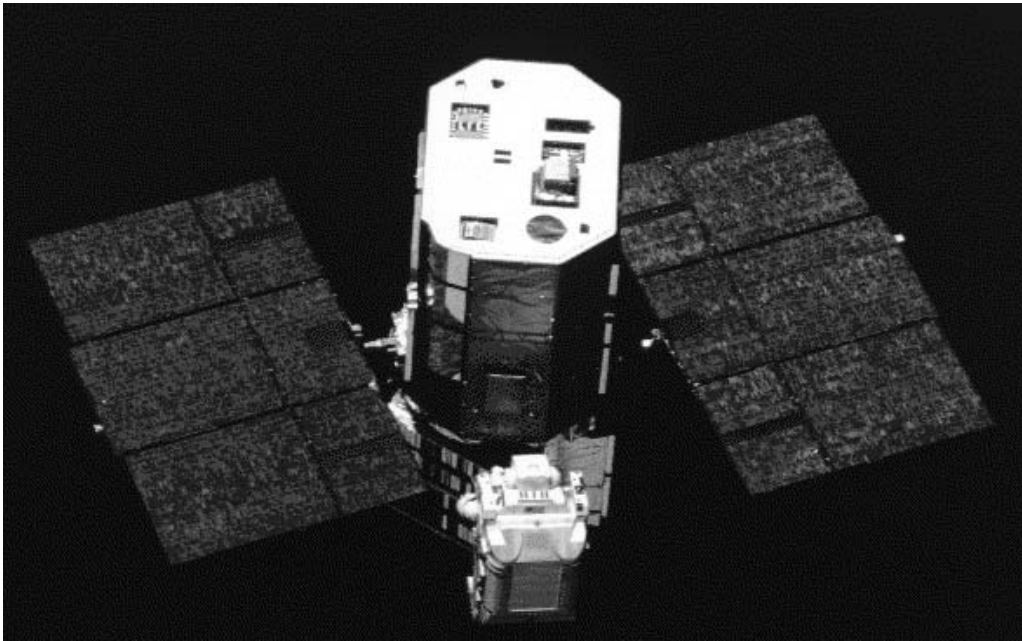


Figure 1.2: The *Solar Maximum Mission (SMM)* satellite was operated during 1980–1989. Some instrument failures occurred early in the mission, such as the position encoder of *FCS* and several gyroscopes. Repairs of the satellite were performed by “Pinky” Nelson and Dick Scobee from the Space Shuttle *Challenger* in April 1984. The approach of the maneuvering astronaut in his flying armchair to the ailing spacecraft is documented in this figure (courtesy of NASA).

tographs during its mission. A comprehensive account of Skylab observations and its scientific results on cool and hot active region loops, as well as on flare loops, is described in the book *Plasma Loops in the Solar Corona* by Bray et al. (1991).

The first solar-dedicated space mission that operated a full solar cycle was the *Solar Maximum Mission (SMM)*, launched on 1980 February 14 and lasting until orbit decay on 1989 December 2 (Fig. 1.2). The *SMM* instrumental package contained a *Gamma-Ray Spectrometer (GRS)* with an energy range of 10 keV–160 MeV, a *Hard X-Ray Burst Spectrometer (HXRBS)* in the energy range of 20–300 keV, a *Hard X-ray Imaging Spectrometer (HXIS)* with moderate spatial resolution (8'' pixels) in the energy range of 3.5–30 keV, two soft X-ray spectrometers [*Bent Crystal Spectrometer (BCS)*, 1.7–3.2 Å, and a *Flat Crystal Spectrometer (FCS)*, 1.4–22 Å], an *Ultraviolet Spectrometer/Polarimeter (UVSP)* in the 1150–3600 Å wavelength range, a white-light *Coronagraph/Polarimeter (CP)* in the 4448–6543 Å wavelength range, and an *Active Cavity Radiometer Irradiance Monitor (ACRIM)* in ultraviolet and infrared wavelengths. *SMM* made a number of scientific discoveries in observing some 12,000 solar flares and several hundred *coronal mass ejections (CME)*, which are lucidly summarized in the book *The Many Faces of the Sun: A Summary of the Results from NASA’s Solar Maximum Mission* by Strong et al. (1999). There was also a Japanese mission (*Hinotori*) flown with similar instrumentation, from 1981 February 21 to 1982 October 11 (see instrumental descriptions in Makishima, 1982 and Takakura et al. 1983a).

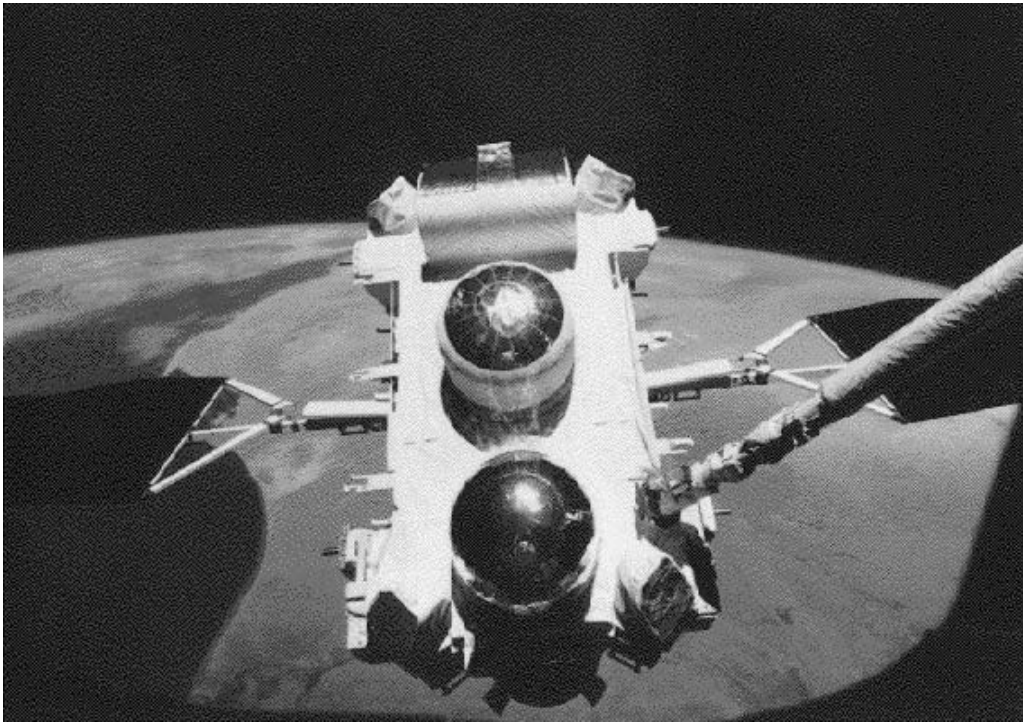


Figure 1.3: Deployment of the *Compton Gamma-Ray Observatory (CGRO)* in 1991 April, photographed from the space shuttle *Atlantis*. The 8 *Large-Area Detectors (LAD)* of the *Burst and Transient Source Experiment (BATSE)* are located at the 8 corners of the spacecraft. The cylindrical detectors on the top are *COMPTEL* and *EGRET*, while *OSSE* is on the far side. The *BATSE* detectors provided for the first time sufficient photon statistics to measure electron time-of-flight delays in solar flares (courtesy of NASA).

In April 1991, the *Compton Gamma-Ray Observatory (CGRO)* was deployed (Fig. 1.3), which was designed to detect gamma-ray bursts from astrophysical and cosmological objects, but actually recorded more high-energy γ -ray and hard X-ray photons from solar flares than from the rest of the universe. In particular the *Burst And Transient Source Experiment (BATSE)* with its high sensitivity (with a collecting area of $2,000 \text{ cm}^2$ in each of the 8 detectors) in the energy range of 25–300 keV (Fishman et al. 1989) delivered unprecedented photon statistics, so that energy-dependent electron time-of-flight delays could be determined in solar flares down to accuracies of a few milliseconds, and thus crucially contributed to a precise localization of particle acceleration sources in solar flares. Also the *Oriented Scintillation Spectrometer Experiment (OSSE)* (Kurfess et al. 1998) provided crucial measurements of γ -ray lines in the energy range of 50 keV to 10 MeV in a number of large X-class flares. *CGRO* recorded a total of some 8000 solar flares during its lifetime. The truck-heavy spacecraft was de-orbited by *NASA* in May 2000 because of gyroscope malfunctions.

The great breakthrough in soft X-ray imaging of the solar corona and flares came with the Japanese mission *Yohkoh* (Ogawara et al. 1991), which contained four instruments (Fig. 1.4): the *Hard X-ray Telescope (HXT)* with four energy channels (14–23

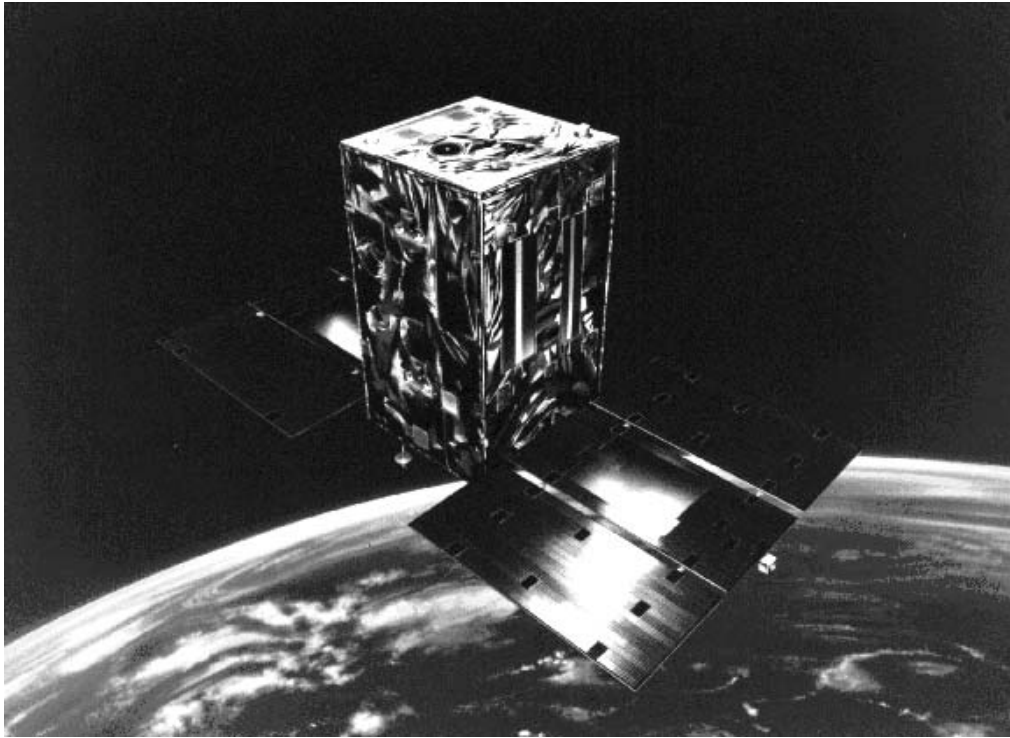


Figure 1.4: On 1991 August 30, the *Yohkoh* satellite was launched into space from the *Kagoshima Space Center (KSC)* in Southern Japan. The *Yohkoh* satellite, meaning “Sunbeam” in Japanese, is a project of the Japanese Institute of Space and Astronautical Science (ISAS) (courtesy of ISAS).

keV, 23–33 keV, 33–53 keV, and 53–93 keV) and a spatial resolution of $\approx 8''$ (Kosugi et al. 1991); the *Soft X-ray Telescope (SXT)* with multiple filters sensitive to temperatures of $T \gtrsim 1.5$ MK, having a spatial resolution of $5''$ in full-disk images and $2.5''$ in partial frames (Tsuneta et al. 1991); a *Wide-Band Spectrometer (WBS)* containing soft X-ray, hard X-ray, and γ -ray spectrometers (Yoshimori et al. 1991); and a *Bent Crystal Spectrometer (BCS)* (Culhane et al. 1991). *Yohkoh* provided a full decade of soft X-ray images from the solar disk and from flares, revealing for the first time the geometry and topology of large-scale magnetic field reconfigurations and magnetic reconnection processes in flares. The satellite lost its pointing during a solar eclipse in December 2001 and reentered in September 2005.

The next major solar mission to observe the Sun from inside out to 30 solar radii in the heliosphere was the *ESA/NASA* jointly-built spacecraft *Solar and Heliospheric Observatory (SoHO)*, launched on 1995 December 2, and still being fully operational at the time of writing. Twelve instrument teams with over 200 co-investigators participate in this mission. The *SoHO* spacecraft includes the following 12 instrument packages: 3 instruments for helioseismology (*GOLF*, *VIRGO*, *SOI/MDI*), 5 instruments for observing the solar atmosphere (*SUMER*, *CDS*, *EIT*, *UVCS*, *LASCO*), and 4 particle detector instruments that monitor the solar wind (*CELIAS*, *COSTEP*, *ERNE*, *SWAN*). Observations of the solar corona are performed by the *Solar Ultraviolet Measurements*

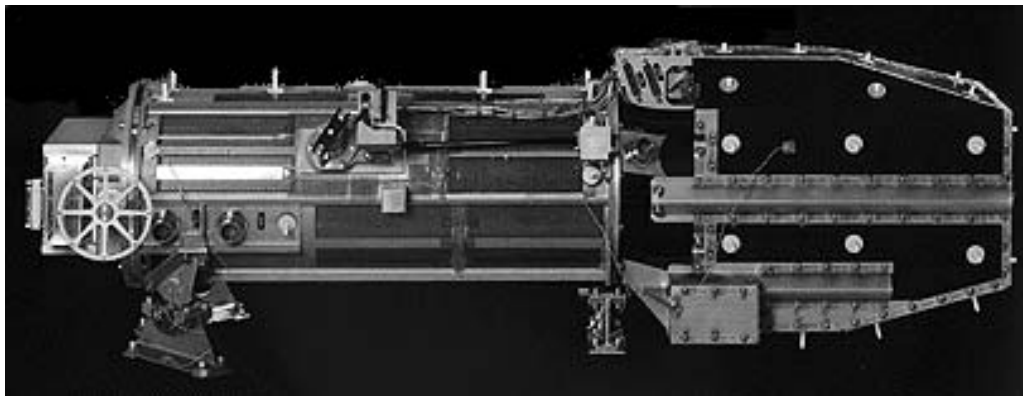


Figure 1.5: The *Extreme-ultraviolet Imaging Telescope (EIT)* on board the *Solar and Heliospheric Observatory (SoHO)* is a normal-incidence, multi-layer telescope (Delaboudinière et al. 1995). It records since 1996 full-disk solar images in multiple filters, sensitive to coronal temperatures of 1–2 MK, with a spatial resolution of $2.5''$ and a cadence of a few hours (courtesy of *EIT* team).

of Emitted Radiation (*SUMER*) telescope and spectrometer in the 500–1610 Å wavelength range (Wilhelm et al. 1995), the *Coronal Diagnostic Spectrometer (CDS)* at 150–800 Å (Harrison et al. 1995), the *Extreme-ultraviolet Imaging Telescope (EIT)* (Fig. 1.5) which takes full-disk images in Fe IX (171 Å), Fe XII (195 Å), Fe XV (284 Å), and He II (304 Å) (Delaboudinière et al. 1995), the *Ultraviolet Coronagraph Spectrometer (UVCS)* which provides spectral line diagnostics between 1 and 3 solar radii, and the *Large Angle Spectroscopic COronagraph (LASCO)* which images the heliosphere from 1.1 to 30 solar radii (Brueckner et al. 1995). Instrument descriptions and first results can be found in Fleck et al. (1995) and Fleck & Svestka (1997). The *SoHO* observatory is a highly successful mission that provided a wealth of data on dynamic processes in the solar corona, which will be described in more detail in the following chapters.

The next solar mission was designed to provide coronal observations with unprecedented high spatial resolution of $\approx 1''$ (with $0.5''$ pixel size), built as a spacecraft with a single telescope, called the *Transition Region And Coronal Explorer (TRACE)* (Fig. 1.6). The *TRACE* telescope was mated on a Pegasus launch vehicle, which launched in 1998 April and is still successfully operating at the time of writing. An instrumental description is provided in Handy et al. (1999). The instrument features a 30-cm Cassegrain telescope with a *field of view (FOV)* of 8.5×8.5 arc minutes and operates in three coronal EUV wavelengths (Fe IX/X, 171 Å; Fe XII/XXIV, 195 Å; and Fe XV, 284 Å), as well as in H I Lyman- α (1216 Å), C IV (1550 Å), UV continuum (1600 Å), and white light (5000 Å). This wavelength set covers temperatures from 6000 K to 10 MK, with the main sensitivity in the 1 – 2 MK range for the EUV filters. *TRACE* has provided us with stunning high-resolution images that reveal intriguing details about coronal plasma dynamics, coronal heating and cooling, and magnetic reconnection processes.

The latest solar mission was launched on 2002 February 5, – a *NASA small ex-*

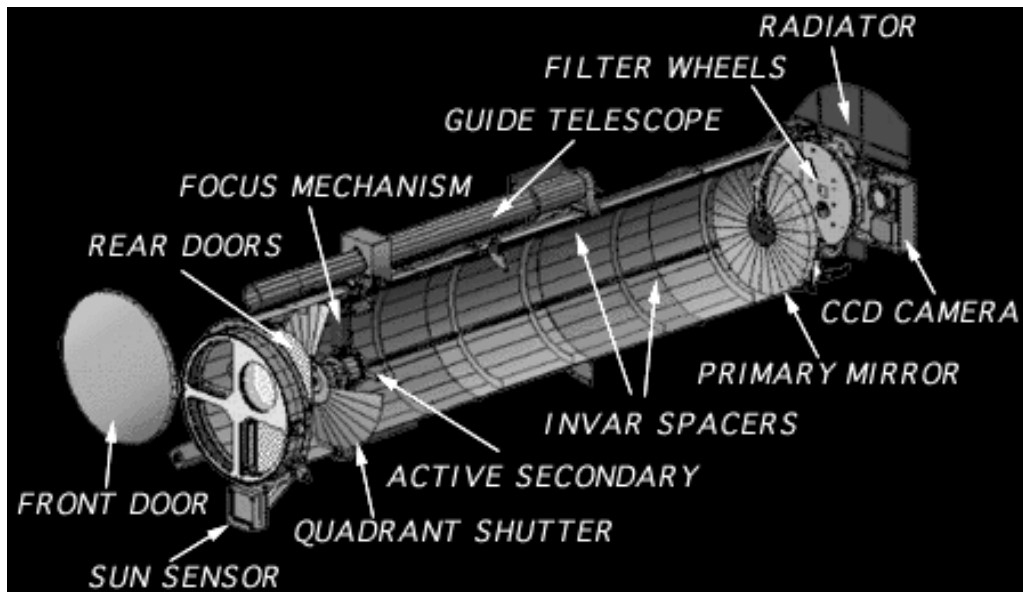


Figure 1.6: A cut-away view of the *Transition Region And Coronal Explorer (TRACE)* telescope is shown. The 30-cm aperture *TRACE* telescope uses four normal-incidence coatings for the EUV and UV on quadrants of the primary and secondary mirrors. The segmented coatings on solid mirrors form identically sized and perfectly co-aligned images. Pointing is internally stabilized to 0.1 arc second against spacecraft jitter. A 1024×1024 CCD detector collects images over an 8.5×8.5 arc minute *field-of-view* (FOV). A powerful data handling computer enables very flexible use of the CCD array including adaptive target selection, data compression, and fast operation for a limited FOV (courtesy of *TRACE* team).

plorer mission (SMEX) called the (Reuven) *Ramaty High Energy Solar Spectroscopic Imager (RHESSI)* (Fig. 1.7), designed to explore the basic physics of particle acceleration and explosive energy release in solar flares. This instrument provides hard X-ray images with the highest ever achieved spatial resolution of $\approx 2.3''$, as well as with the highest energy resolution (achieved by germanium-cooled detectors). An instrumental description of the *RHESSI* spacecraft can be found in Lin et al. (1998b, 2002). Although this mission was launched late in solar cycle XXIII, it has already recorded 7500 solar flares during the first year.

Progress in the physical understanding of the structure and dynamics of the solar corona is mainly driven by space-based observations in EUV, soft X-rays, and hard X-rays, obtained by the high-resolution imagers that were flown over the last decade. However, very valuable and complementary observations have also been produced by ground-based observatories. There are essentially two wavelength regimes that are observable from ground and provide information on the solar corona (i.e., optical and radio wavelengths). Imaging radio observations of the solar corona have mainly been accomplished by the *Culgoora radioheliograph* in Australia (1967–1984), the *Nançay radioheliograph* in France (since 1977), the *Very Large Array (VLA)* in New Mexico (since 1980), the *Owens Valley Radio Observatory (OVRO)* in California (since 1978),

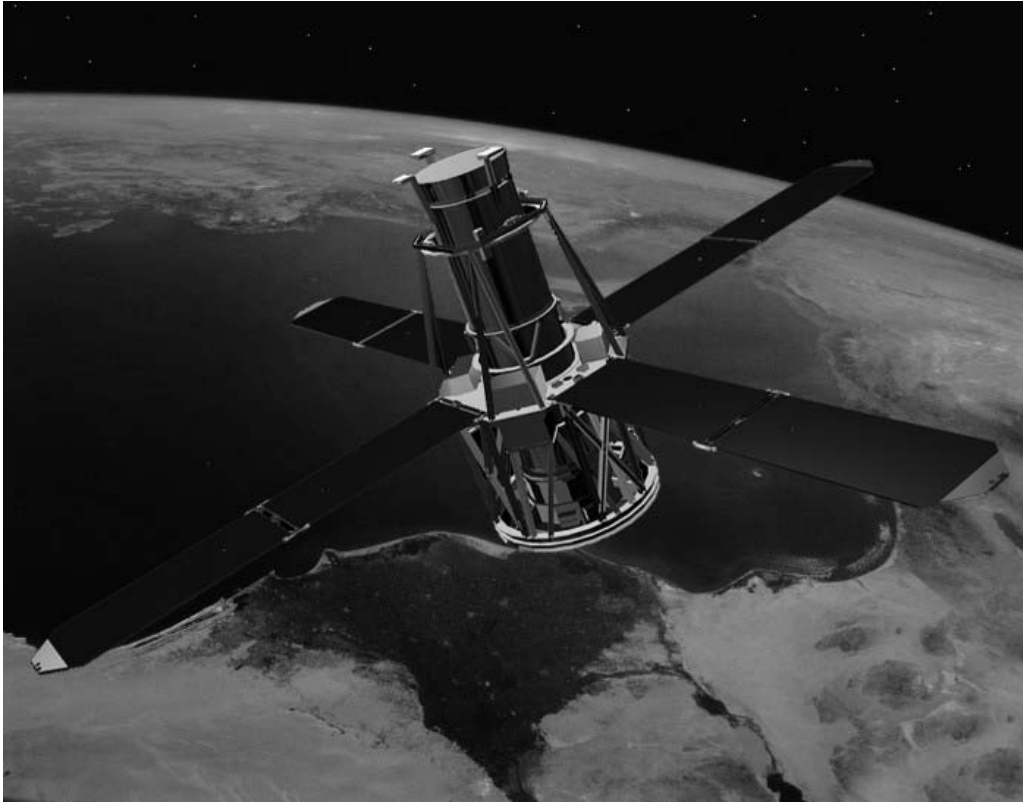


Figure 1.7: The *Ramaty High Energy Solar Spectroscopic Imager (RHESSI)* is a spinning spacecraft that contains a single instrument, a rotation-modulated collimator with 9 germanium-cooled detectors (courtesy of *RHESSI* Team).

RATAN-600 in Russia (since 1972), and the *Nobeyama Radio Observatory* in Japan (since 1992). There is also a larger number of radio spectrometers distributed all around the world, which complement imaging radiotelescopes with dynamic spectra of high temporal and spectral resolution.

1.2 Nomenclature of Coronal Phenomena

We start now with a tour of coronal phenomena, describing them first by their morphological appearance in observed images, giving a more physical definition and quantitative characterization in the following chapters of the book. For an illustrated glossary of phenomena in solar and solar-terrestrial physics see also Bruzek & Durrant (1977).

It is customary to subdivide the solar corona into three zones, which all vary their size during the solar cycle: (1) active regions, (2) quiet Sun regions, and (3) coronal holes.

Active regions: Like cities on the Earth globe, active regions on the solar surface harbor most of the activity, but make up only a small fraction of the total surface area. Active regions are located in areas of strong magnetic field concentrations, visible as

sunspot groups in optical wavelengths or magnetograms. Sunspot groups typically exhibit a strongly concentrated leading magnetic polarity, followed by a more fragmented trailing group of opposite polarity. Because of this bipolar nature active regions are mainly made up of closed magnetic field lines. Due to the permanent magnetic activity in terms of magnetic flux emergence, flux cancellation, magnetic reconfigurations, and magnetic reconnection processes, a number of dynamic processes such as plasma heating, flares, and coronal mass ejections occur in active regions. A consequence of plasma heating in the chromosphere are upflows into coronal loops, which give active regions the familiar appearance of numerous filled loops, which are hotter and denser than the background corona, producing bright emission in soft X-rays and extreme ultraviolet (EUV) wavelengths. In the *Yohkoh* soft X-ray image shown in Fig. 1.8, active regions appear in white. The heliographic position of active regions is typically confined within latitudes of $\pm 40^\circ$ from the solar equator.

Quiet Sun: Historically, the remaining areas outside of active regions were dubbed *quiet Sun* regions. Today, however, many dynamic processes have been discovered all over the solar surface, so that the term *quiet Sun* is considered as a misnomer, only justified in relative terms. Dynamic processes in the quiet Sun range from small-scale phenomena such as network heating events, nanoflares, explosive events, bright points, and soft X-ray jets, to large-scale structures, such as transequatorial loops or coronal arches. The distinction between active regions and quiet Sun regions becomes more and more blurred because most of the large-scale structures that overarch quiet Sun regions are rooted in active regions. A good working definition is that quiet Sun regions encompass all closed magnetic field regions (excluding active regions), clearly demarcating the quiet Sun territory from coronal holes, which encompass open magnetic field regions.

Coronal holes: The northern and southern polar zones of the solar globe have generally been found to be darker than the equatorial zones during solar eclipses. Max Waldmeier thus coined those zones as “Koronale Löcher” (in German, i.e., *coronal holes*). Today it is fairly clear that these zones are dominated by open magnetic field lines, that act as efficient conduits for flushing heated plasma from the corona into the solar wind, if there are any chromospheric upflows at their footpoints. Because of this efficient transport mechanism, coronal holes are empty of plasma most of the time, and thus appear much darker than the quiet Sun, where heated plasma upflowing from the chromosphere remains trapped until it cools down and precipitates back to the chromosphere.

Like our Earth atmosphere displays a large variety of cloud shapes, from bulky stratocumuli to fine-structured cirrus clouds, the solar corona exhibits an equally rich menagerie of loop morphologies, which can reveal important clues about the underlying magnetic reconnection and reconfiguration processes. Pointed and cusp-shaped structures may pinpoint coronal nullpoints of X-type magnetic reconnection points, while circular geometries may indicate relaxed, near-dipolar magnetic field geometries. In Fig. 1.9 we show some characteristic coronal structures that are typically seen in soft X-ray images (Acton et al. 1992).

Helmet streamers: Streamers (e.g., Fig. 1.9[A]) are huge, long-lived, radially oriented structures that extend from the base of the corona out to several solar radii. A

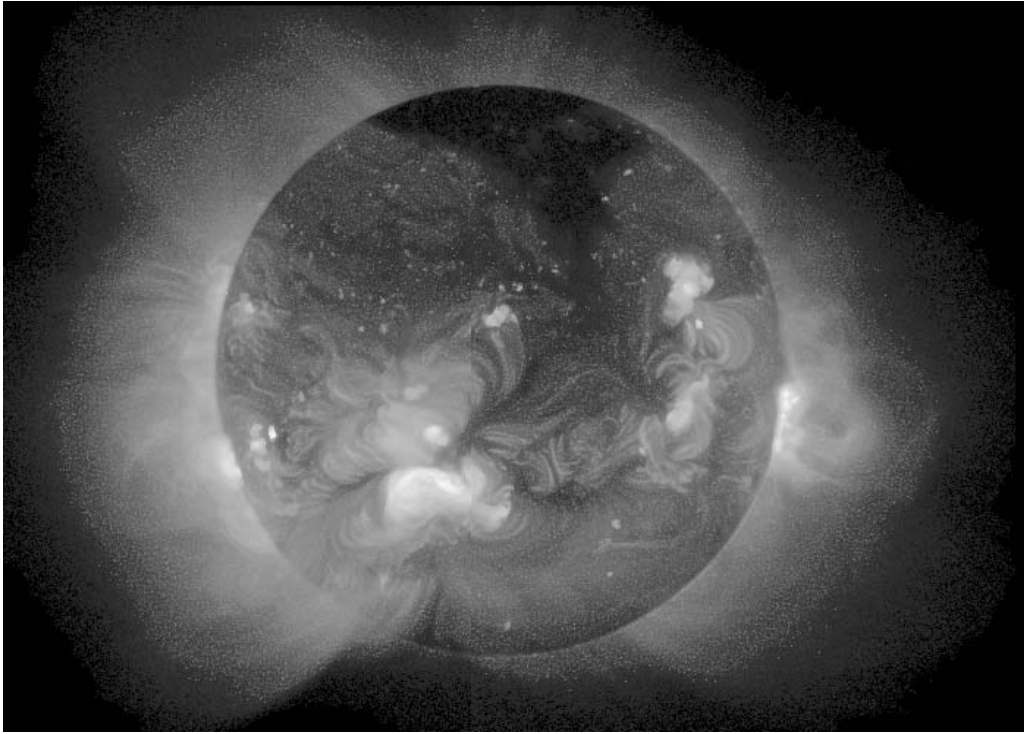


Figure 1.8: Soft X-ray image of the extended solar corona recorded on 1992 August 26 by the *Yohkoh Soft X-ray Telescope (SXT)*. The image was made up from two pointings of the spacecraft, one to the east and one to the west, to capture the distant corona far above the Sun’s limb (courtesy of *Yohkoh Team*).

subclass are *helmet streamers*, which are connected with active regions and are centered over prominences (above the limb) or filaments (on the disk). The lower part contains closed field lines crossing a neutral line, while the upper part turns into a cusp-shaped geometry, giving the appearance of a “helmet”. Above the helmet, a long, straight, near-radial stalk continues outward into the heliosphere, containing plasma that leaks out from the top of the helmet where the thermal pressure starts to overcome the magnetic confinement (plasma- β parameter $\gtrsim 1$).

Loop arcades: Regions of opposite magnetic polarity can sometimes have a quite large lateral extent, so that dipolar loops can be found lined up perpendicularly to a neutral line over a large distance, with their footpoints anchored in the two ribbons of opposite magnetic polarity on both sides of the neutral line. Such a loop arcade is shown end-on in Fig. 1.9(B), which illustrates that the cross section of an arcade can appear like a single loop.

Soft X-ray jets: If heated plasma flows along an open field line, it is called a *soft X-ray jet*, which can have the form of a linear structure, sometimes slightly bent. Such a jet feature is shown in Fig. 1.9(C), which grew with a velocity of 30 km s^{-1} to a length of 200 Mm. Such jet features are visible until the flow fades out or the structure erupts.

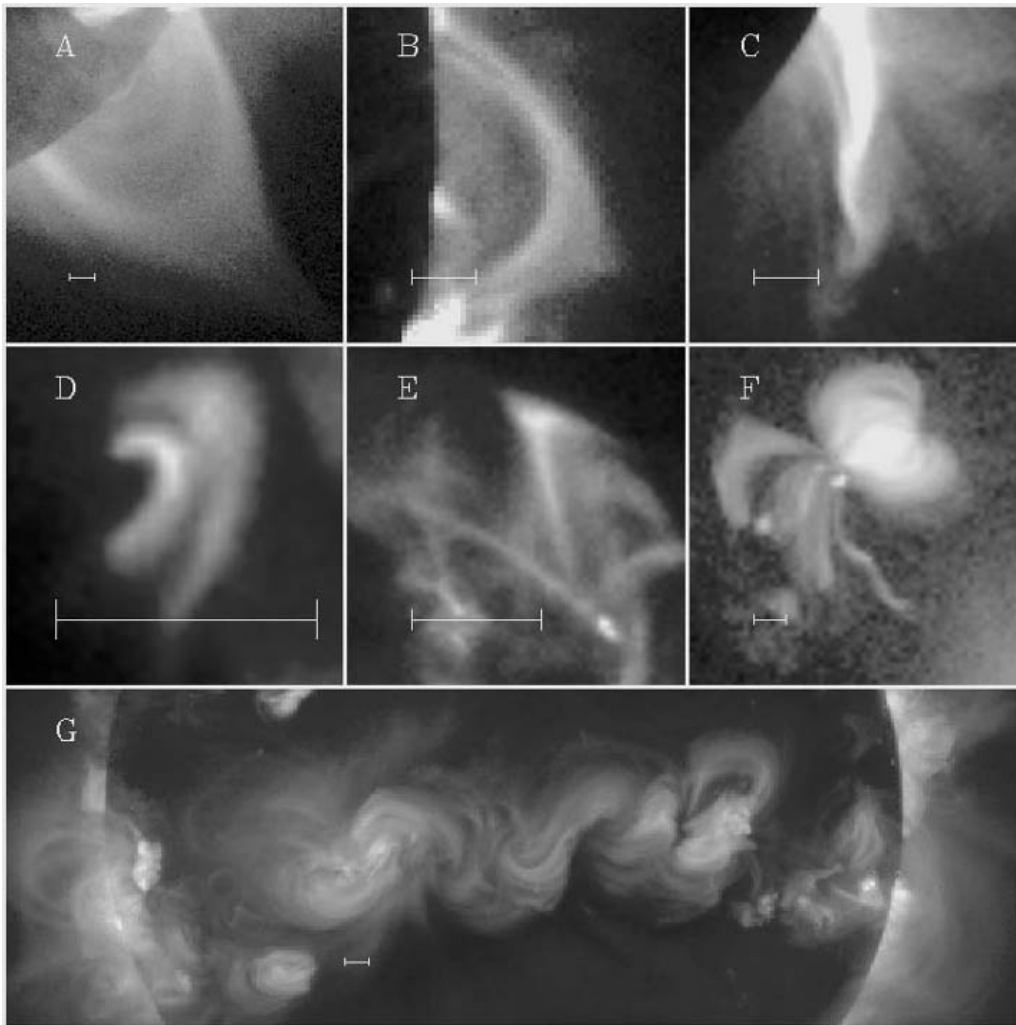


Figure 1.9: A collection of soft X-ray structures is shown, recorded with *SXT/Yohkoh*, from 1991 October 3 to 1992 January 25, described in Acton et al. (1992). The images exemplify the variety of solar coronal features seen in soft X-rays: A) Large helmet-type structure; B) arcade of X-ray loops seen end-on; C) dynamic eruptive feature which grew at a velocity of about 30 km s^{-1} ; D) a pair of small symmetrical flaring loops; E) two cusped loops with heating in the northern loop; F) a tightly beamed X-ray jet towards the southwest at 200 km s^{-1} ; and G) the sinuous magnetic connection between active regions (courtesy of *Yohkoh* Team).

Postflare loops: Flare loops become bright in soft X-rays after they become filled up by upflowing heated plasma, a process that is dubbed *chromospheric evaporation*, driven by intense chromospheric heating at the loop footpoints from precipitating non-thermal particles or thermal conduction fronts. Flare (or postflare) loops trace out dipole-like magnetic field lines, after relaxation from flare-related magnetic reconnection processes. A pair of flaring loops are shown in Fig. 1.9(D), where the smaller flaring loop has a height of 10 Mm and a footpoint separation of 18 Mm.

Cusp-shaped loops: Loop segments with a pointed shape at the top, are also called *cusps* (Fig. 1.9[E]). Such cusps represent deviations from dipole-like magnetic field lines and thus indicate some dynamic processes. Cusps are expected in X-type reconnection geometries, and thus may occur right after a magnetic reconnection process, if the chromospheric plasma filling process happens sufficiently fast before the loop relaxes into a dipole-like (near-circular) geometry. The cusp of the northern loop shown in Fig. 1.9(E) is particularly bright, and thus may even indicate local heating at the cusp.

Multiple arcades: It is not uncommon that multiple neutral lines occur in active regions, which organize the magnetic field into multiple arcades side-by-side, as shown in the “bow-tie” structure in Fig. 1.9(F). Multiple arcades can lead to quadrupolar magnetic structures, which play a key role in eruptive processes, because a coronal magnetic nullpoint occurs above such neighboring magnetic flux systems, which aids in opening up the field by reconnecting away the overlying closed field lines (according to the so-called *magnetic breakout model* (Antiochos et al. 1999b)).

Sigmoid structures: If a dipole field is sheared, the field lines deform into S-shaped geometries, which are also called *sigmoids*. A string of sigmoid-shaped field line bundles are shown in Fig. 1.9(G), stringing together a series of sheared active regions along the solar equator. Sigmoids can imply nonpotential magnetic fields that have an excess energy over the potential field configuration, and thus may contain free energy to spawn a flare or coronal mass ejection. It is not clear yet whether the eruptive phase is initiated by a kink instability of the twisted field lines or by another loss-of-equilibrium process.

The foregoing inventory describes quasi-stationary or slowly varying coronal structures. Rapidly varying processes, which all result from a loss of equilibrium, are also called eruptive processes, such as flares, coronal mass ejections, or small-scale variability phenomena.

Flares: A flare process is associated with a rapid energy release in the solar corona, believed to be driven by stored nonpotential magnetic energy and triggered by an instability in the magnetic configuration. Such an energy release process results in acceleration of nonthermal particles and in heating of coronal/chromospheric plasma. These processes emit radiation in almost all wavelengths: radio, white light, EUV, soft X-rays, hard X-rays, and even γ -rays during large flares.

Microflares and nanoflares: The energy range of flares extends over many orders of magnitude. Small flares that have an energy content of 10^{-6} to 10^{-9} of the largest flares fall into the categories of microflares and *nanoflares*, which are observed not only in active regions, but also in quiet Sun regions. Some of the microflares and nanoflares have been localized to occur above the photospheric network, and are thus also dubbed *network flares* or *network heating events*. There is also a number of small-scale phenomena with rapid time variability for which it is not clear whether they represent miniature flare processes, such as *active region transients*, *explosive events*, *blinkers*, etc. It is conceivable that some are related to *photospheric* or *chromospheric* magnetic reconnection processes, in contrast to flares that always involve *coronal* magnetic reconnection processes.

Coronal mass ejections (CME): Large flares are generally accompanied by eruptions of mass into interplanetary space, the so-called *coronal mass ejections (CME)*.

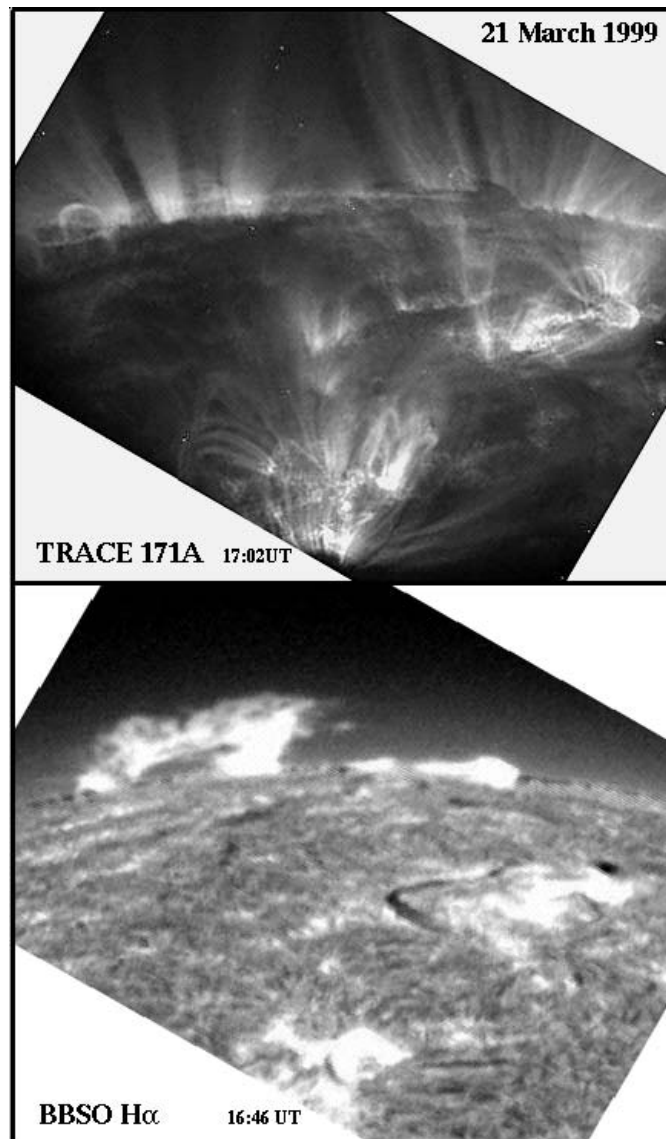


Figure 1.10: These images (taken on 1999 March 21) compare the corona seen in EUV (top panel: *TRACE*, 171 Å, $T=1$ MK) and the chromosphere seen in $H\alpha$ (bottom panel: *Big Bear Solar Observatory (BBSO)*, $T=10,000$ K). The cool filaments (on the disk) and prominences (above the limb) show up as bright structures in $H\alpha$ (bottom frame), but as dark, absorbing features in EUV (top frame) (courtesy of *TRACE* and *BBSO*).

Flares and CMEs are two aspects of a large-scale magnetic energy release, but the two terms evolved historically from two different observational manifestations (i.e., *flares* denoting mainly the emission in hard X-rays, soft X-rays, and radio, while *CMEs* being referred to the white-light emission of the erupting mass in the outer corona and heliosphere). Recent studies, however, clearly established the co-evolution of both processes triggered by a common magnetic instability.

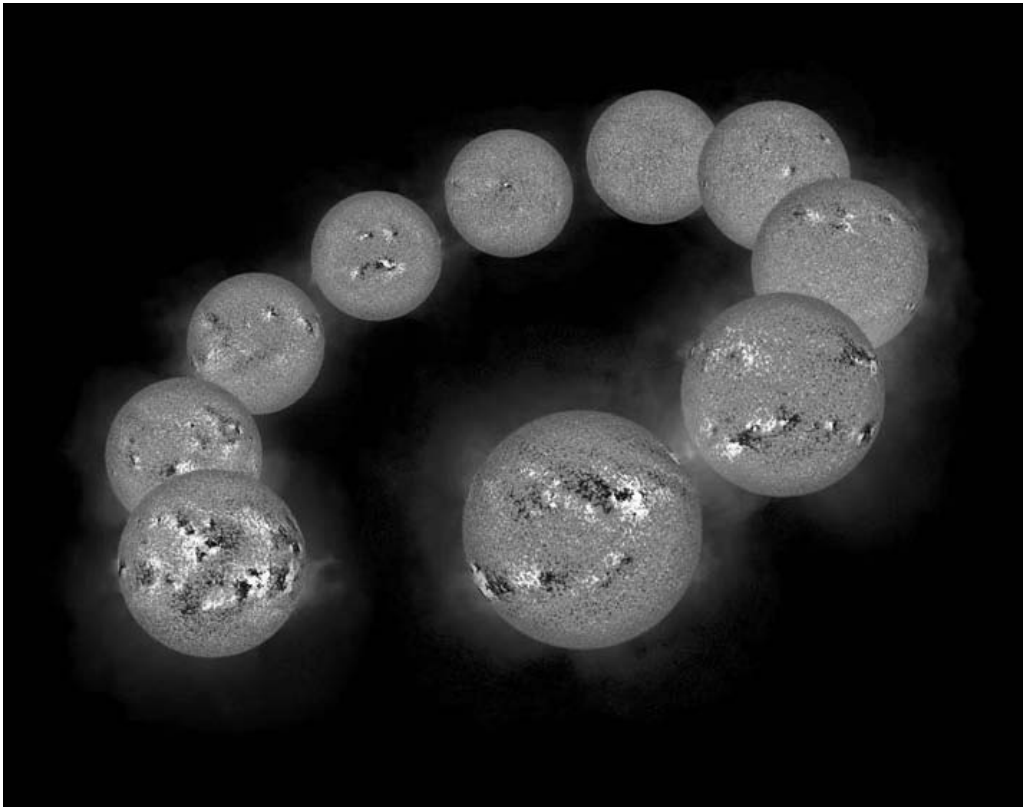


Figure 1.11: Ten maps of photospheric magnetograms are shown, spanning a period of almost a solar cycle, from 1992 January 8 to 1999 July 25, recorded with the Vacuum Telescope of the *National Solar Observatory (NSO)* at *Kitt Peak National Observatory (KPNO)*, Tucson, Arizona. White and black colors indicate positive and negative magnetic polarity (of the longitudinal magnetic field component B_{\parallel}), while grey indicates the zero field (courtesy of KPNO).

Filaments and prominences: A filament is a current system above a magnetic neutral line that builds up gradually over days and erupts during a flare or CME process. Historically, filaments were first detected in $H\alpha$ on the solar disk, but later they were also discovered in He 10,830 Å and in other wavelengths. On the other side, erupting structures above the limb seen in $H\alpha$ and radio wavelengths were called *prominences*. Today, both phenomena are unified as an identical structure, with the only significant difference being that they are observable on the disk in absorption (filaments) and above the limb in emission (prominences), (e.g., see Fig. 1.10).

1.3 The Solar Magnetic Cycle

The solar magnetic cycle of about 11 years, during which the magnetic polarity of the global solar magnetic field is reversed, modulates the total radiation output in many wavelengths in a dramatic way. A full cycle of 22 years, after which the original magnetic configuration is restored, is called a *Hale cycle*. The total magnetic flux

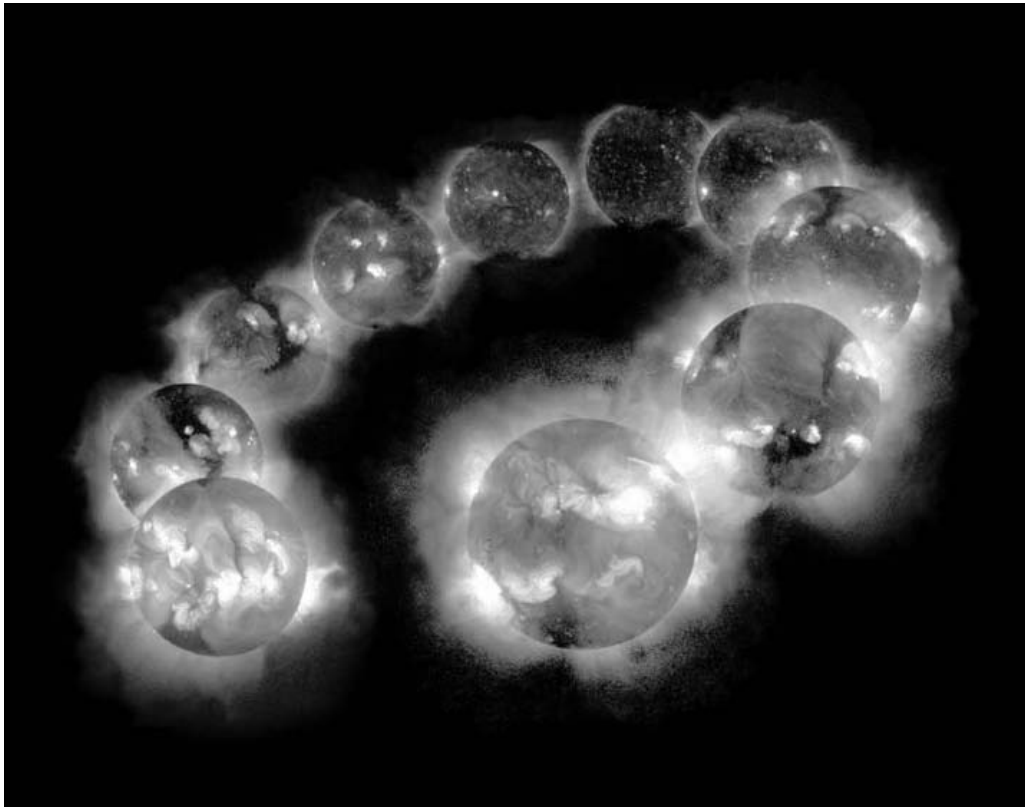


Figure 1.12: Ten soft X-ray maps of the Sun, covering the same time interval of almost a full solar cycle as the magnetograms shown in Fig. 1.11, observed with the *Solar X-ray telescope (SXT)* on the *Yohkoh* spacecraft (courtesy of Yohkoh Team).

reaches a maximum during the peak of a cycle and drops to a low level during the minimum of the cycle (see magnetograms in Fig. 1.11). During the solar cycle, the magnetic flux varies by a factor of ≈ 8 in active regions, by a factor of ≈ 2 in ephemeral regions, and even in anti-phase in small regions (Hagenaar et al. 2003). Since many radiation mechanisms are directly coupled to the dissipation of magnetic energy and related plasma heating, the radiation output in these wavelengths is correspondingly modulated from solar maximum to minimum (e.g., in soft X-rays, hard X-rays, and radio wavelengths). This can clearly be seen from the sequence of Yohkoh soft X-ray images shown in Fig. 1.12.

Although the modulation of optical emission during a cycle is much less dramatic than in X-rays, the magnetic solar cycle was discovered long ago, based on the increase and decrease of sunspots. The east-west orientation of the magnetic field in active regions was found to be opposite in the northern and southern hemispheres, switching for every 11-year cycle, known as *Hale's polarity law*. During a cycle, the active regions migrate from high latitudes ($\approx 40^\circ$) towards lower latitudes ($\approx 10^\circ$) near the equator, leading to the famous *butterfly diagram of sunspots* (Spörer's law), when their latitudinal position is plotted as a function of time.

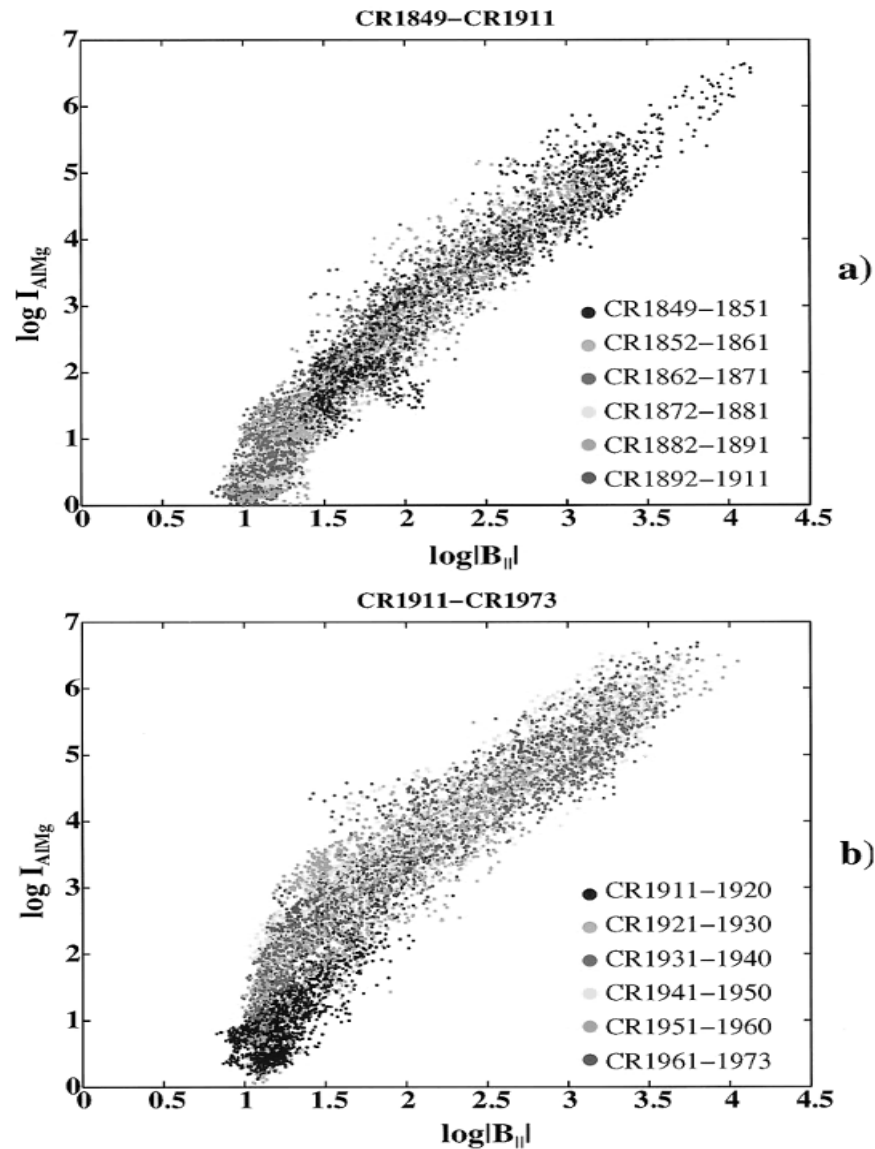


Figure 1.13: Scatter plots of the soft X-ray intensity from *SXT* (Yohkoh) data in the AlMg filter as a function of the magnetic flux (from the Kitt Peak Observatory) in the natural logarithmic scale for the latitudinal zone from -55° to $+55^\circ$ for two periods: (a) 1991 November 11 to 1996 July 25, and (b) 1996 June 28 to 2001 March 13. Different subperiods are marked by different grey tones. The color-coding in terms of Carrington rotation numbers is shown in the figures (Benevolenskaya et al. 2002).

The cyclic evolution of the sunspots can be understood in terms of a reversal of the global solar magnetic field, which evolves from an initial poloidal field towards a toroidal field under the influence of differential rotation, according to a model by Horace W. Babcock proposed in 1961. In recent versions of this scenario, the cause of the solar cycle is a dynamo-like process that is driven by the internal magnetic field in the tachocline at the bottom of the convection zone. There a strong magnetic field in the

order of 100,000 G is periodically strengthened and weakened, from which occasionally buoyant magnetic fluxtubes arise and emerge at the photospheric surface, visible as bipolar sunspot pairs. The differential surface rotation shears the new emerging fields gradually into a more toroidal field, until surface diffusion by granular convection breaks up the field and meridional flows transport the fragments towards the poles. The surface diffusion neutralizes the toroidal field component increasingly during the decay of the cycle, so that a weak poloidal global field is left at the cycle minimum. When the internal dynamo strengthens the tachocline field again, the rate of buoyant fluxtubes increases and the cycle starts over.

The coupling of the photospheric magnetic field (Fig. 1.11) to the coronal soft X-ray emission (Fig. 1.12) has been quantitatively investigated (e.g., Fisher et al. 1998 and Benevolenskaya et al. 2002), resulting in an unambiguous correlation between the two quantities, when sampled over a solar cycle (Fig. 1.13). It was found that the soft X-ray intensity, I_{SXR} , scales approximately with the square of the magnetic field, B^2 , and thus the soft X-ray intensity can be considered as a good proxy of the magnetic energy ($\varepsilon_m = B^2/8\pi$). Slightly different powerlaw values have been found for the solar maximum and minimum (Benevolenskaya et al. 2002),

$$I_{SXR} \propto \langle |B_{\parallel}| \rangle^n \begin{cases} n = 1.6 - 1.8 & \text{solar maximum} \\ n = 2.0 - 2.2 & \text{solar minimum} . \end{cases} \quad (1.3.1)$$

The soft X-ray flux is an approximate measure of the energy rate (E_H) that is deposited into heating of coronal plasma according to this positive correlation. On the other hand, global modeling of magnetic fields and soft X-ray flux from the Sun and cool stars yields a more linear relationship, $E_H \propto B^{1.0 \pm 0.5}$ (e.g., Schrijver & Aschwanden, 2002). It is conceivable that the positive correlation applies more generally to all energy dissipation processes in the solar corona (i.e., that the processes of coronal heating, flare plasma heating, and particle acceleration are ultimately controlled by the amount of magnetic energy that emerges through the solar surface, modulated by about two orders of magnitude during a solar cycle).

1.4 Magnetic Field of the Solar Corona

The solar magnetic field controls the dynamics and topology of all coronal phenomena. Heated plasma flows along magnetic field lines and energetic particles can only propagate along magnetic field lines. Coronal loops are nothing other than conduits filled with heated plasma, shaped by the geometry of the coronal magnetic field, where cross-field diffusion is strongly inhibited. Magnetic field lines take on the same role for coronal phenomena as do highways for street traffic. There are two different magnetic zones in the solar corona that have fundamentally different properties: open-field and closed-field regions. Open-field regions (white zones above the limb in Fig. 1.14), which always exist in the polar regions, and sometimes extend towards the equator, connect the solar surface with the interplanetary field and are the source of the *fast solar wind* ($\approx 800 \text{ km s}^{-1}$). A consequence of the open-field configuration is efficient plasma transport out into the heliosphere, whenever chromospheric plasma is heated at the footpoints. Closed-field regions (grey zones in Fig. 1.14), in contrast, contain

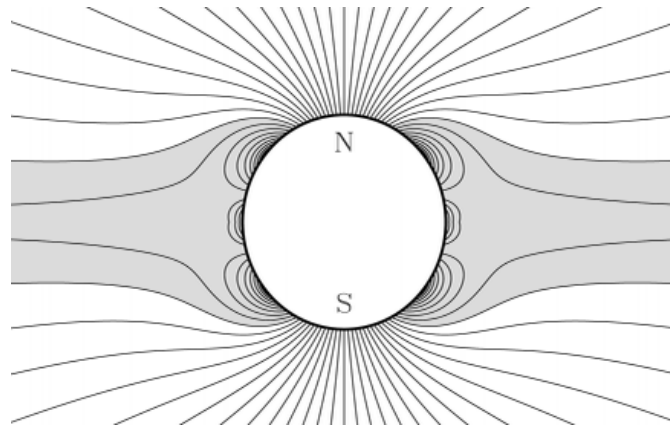


Figure 1.14: Depiction of lines of magnetic force in the semi-empirical multipole-current sheet coronal model of Banaszkiewicz et al. (1998). The high-speed solar wind fills the unshaded volume above the solar surface (Cranmer, 2001).

mostly closed field lines in the corona up to heights of about one solar radius, which open up at higher altitudes and connect eventually to the heliosphere, but produce a *slow solar wind* component of $\approx 400 \text{ km s}^{-1}$. It is the closed-field regions that contain all the bright and overdense coronal loops, produced by filling with chromospheric plasma that stays trapped in these closed field lines. For loops reaching altitudes higher than about one solar radius, plasma confinement starts to become leaky, because the thermal plasma pressure exceeds the weak magnetic field pressure which decreases with height (plasma- β parameter > 1).

The magnetic field on the solar surface is very inhomogeneous. The strongest magnetic field regions are in sunspots, reaching field strengths of $B = 2000 - 3000 \text{ G}$. Sunspot groups are dipolar, oriented in an east-west direction (with the leading spot slightly closer to the equator) and with opposite leading polarity in both hemispheres, reversing for every 11-year cycle (*Hale's laws*). Active regions and their plages comprise a larger area around sunspots, with average photospheric fields of $B \approx 100 - 300 \text{ G}$ (see Fig. 1.11), containing small-scale pores with typical fields of $B \approx 1100 \text{ G}$. The background magnetic field in the quiet Sun and in coronal holes has a net field of $B \approx 0.1 - 0.5 \text{ G}$, while the absolute field strengths in resolved elements amount to $B = 10 - 50 \text{ G}$. Our knowledge of the solar magnetic field is mainly based on measurements of Zeeman splitting in spectral lines, while the coronal magnetic field is reconstructed by extrapolation from magnetograms at the lower boundary, using a potential or force-free field model. The extrapolation through the chromosphere and transition region is, however, uncertain due to unknown currents and non-force-free conditions. The fact that coronal loops exhibit generally much less expansion with height than potential-field models underscores the inadequacy of potential-field extrapolations. Direct measurements of the magnetic field in coronal heights are still in their infancy.

An empirical compilation of coronal magnetic field measurements is given in the paper of Dulk & McLean (1978), reproduced in Fig. 1.15. This compilation combines

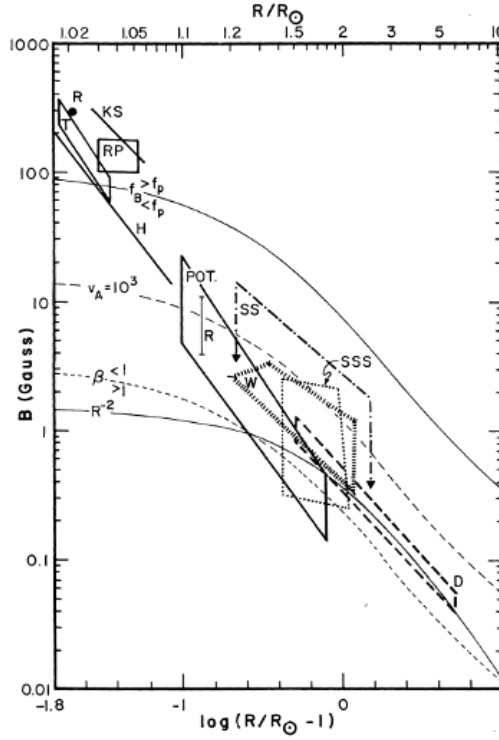


Figure 1.15: Compilation of coronal magnetic field measurements (Dulk & McLean, 1978).

the following measurement methods of the magnetic field: (1) in situ measurements by spacecraft at $\gtrsim 0.5$ AU; (2) Zeeman effect in active region prominences; (3) extrapolations from photospheric magnetograms; (4) microwave radio bursts with gyroresonance emission; (5) decimetric bursts that involve a frequency drift related to the Alfvén speed; (6) metric type II radio bursts, which have a shock speed related to the Alfvénic Mach number; and (7) type III bursts that show a circular polarization, which depends on the refractive index and local magnetic field. Although the magnetic field strength varies 1 – 2 orders of magnitude at any given height (see Fig. 1.15), Dulk & McLean (1978) derived an empirical formula that approximately renders the average decrease of the magnetic field with height between 1.02 and 10 solar radii,

$$B(R) = 0.5 \left(\frac{R}{R_{\odot}} - 1 \right)^{-1.5} \text{ G} \quad (1.02 \lesssim R/R_{\odot} \lesssim 10). \quad (1.4.1)$$

Of course, the variation of the magnetic field strength by 1 – 2 orders of magnitude is mainly caused by the solar cycle (see Fig. 1.13). Alternative methods to measure the coronal magnetic field directly employ the effects of Faraday rotation, the polarization of free-free emission, Hanle effect in H Lyman- α , or Stokes polarimetry in infrared lines.

In order to give a practical example of how the magnetic field varies in typical active region loops, we show the height dependence $B(h)$ of calculated potential-field lines (using *MDI/SoHO* magnetograms) that are co-spatial with some 30 active regions

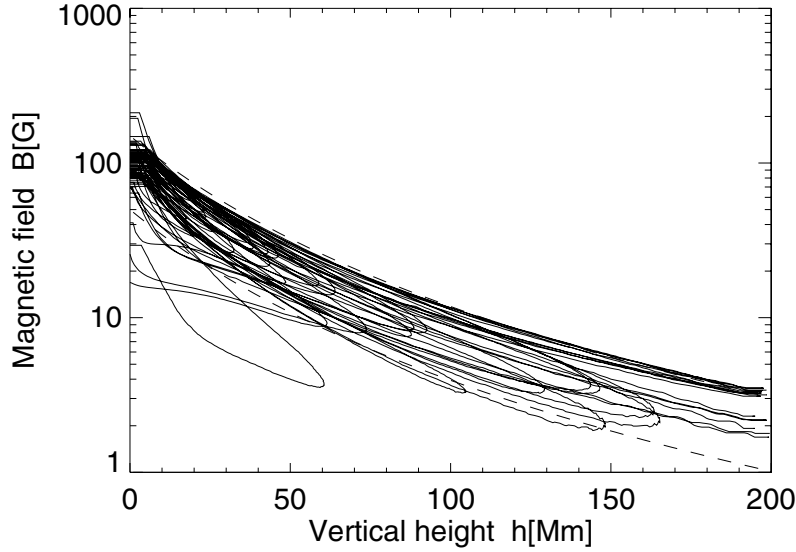


Figure 1.16: Magnetic field extrapolations of 30 loops in an active region based on a *MDI/SoHO* magnetogram (Aschwanden et al. 1999a).

loops traced from *EIT/SoHO* 171 Å images (Aschwanden et al. 1999a). These active region loops reach heights of $h \approx 50 - 200$ Mm. The photospheric magnetic field strength at their footpoints varies in the range of $B_{foot} \approx 20 - 200$ G (averaged over a pixel of the MDI magnetogram), but drops below $B \lesssim 10$ G for heights of $h \gtrsim 100$ Mm. The height dependence of the magnetic field can be approximated with a dipole model (dashed lines in Fig. 1.16),

$$B(h) = B_{foot} \left(1 + \frac{h}{h_D} \right)^{-3}, \quad (1.4.2)$$

with a mean dipole depth of $h_D \approx 75$ Mm. Of course, the dipole approximation is contingent on the potential-field model. Alternatively, if one assumes a constant magnetic flux $\Phi(s) = B(s)A(s)$ along the loop, as the almost constant cross-sectional area $A(s)$ of observed loops suggests, one might infer in the corona an almost constant field with height, $B(h) \approx const$, while the largest magnetic field decrease occurs in the chromospheric segment, which expands like a canopy above the photospheric footpoint. It is therefore imperative to develop direct measurement methods of the coronal field to decide between such diverse models.

1.5 Geometric Concepts of the Solar Corona

Solar or stellar atmospheres are generally characterized in lowest order by spherical shells, with a decreasing density as a function of the radial distance from the surface. The spherical structure is, of course, a result of the gravitational stratification, because the gravitational potential $U(r)$ is only a function of the radial distance r from the mass center of the object. The gravitational stratification, which just makes the simplest

assumption of pressure equilibrium and homogeneity, is a useful basic concept of the average radial density structure for portions of the atmosphere that are horizontally quasi-homogeneous.

The solar corona, however, is highly inhomogeneous, due to the structuring of the magnetic field. The decisive parameter is the ratio of the thermal pressure p_{th} to the magnetic pressure p_{mag} , also called the plasma- β parameter (see §1.8). In the major part of the solar corona, the value of the plasma- β parameter is less than unity, which constitutes a rigorous topological constraint, inasmuch as the thermal pressure is insufficient to warrant horizontal stratification across the magnetic field. This inhibition of cross-field transport has the natural consequence that every plasma that streams from the chromosphere to the corona, traces out bundles of magnetic field lines, with cross sections that are roughly determined by the geometric area where the chromospheric upflows pass the boundary of $\beta \lesssim 1$, which is generally at heights of the transition region. This topological structuring of the corona has the nice property that the radiating coronal plasma can be used to delineate the 3D coronal magnetic field $\mathbf{B}(x, y, z)$, but it also produces a highly inhomogeneous density structure, which is more difficult to model than a homogeneous atmosphere.

The evolution of our perception of the topological structure of the solar corona is depicted in Fig. 1.17. While the concept of gravitationally stratified spheres seemed to be adequate to model the average density structure of the solar corona in the 1950s, the concept of magnetic structuring into horizontally separated fluxtubes, which essentially represent isolated “mini-atmospheres”, was introduced in the 1980s. In the last decade before 2000, the high-resolution images from spacecraft observations revealed a spatially highly inhomogeneous and temporally dynamic corona, which is constantly stirred up by dynamic processes such as heated chromospheric upflows, cooling downflows, magnetic reconfigurations, and interactions with waves. The trend is clear, our picture evolved from stationary and spherical symmetry away towards dynamic and highly inhomogeneous topologies.

So we can conceive the topology of the solar corona by structures that are aligned with the magnetic field. There are two types of magnetic field lines: *closed field lines* that start and end at the solar surface, and *open field lines* which start at the solar surface and end somewhere in interplanetary space. Also for theoretical reasons, open field lines close over very large distances, to satisfy Maxwell’s equation $\nabla \cdot \mathbf{B} = 0$, which states that there are no static sources of magnetic field in the absence of magnetic monopoles. The appearance of closed magnetic field lines loaded with over-dense plasma, with respect to the ambient density, has led to the familiar phenomenon of *coronal loops*, which are ubiquitous, and most conspicuously seen in active regions, but can also be discerned everywhere in quiet Sun regions, except in coronal holes near the poles.

A loop structure can essentially be parametrized in a 1D coordinate system given by the central magnetic field line. However, the extent of the transverse cross section is less well defined. What a telescope perceives as a cross-sectional area, depends very much on the angular resolution. Theoretically, a loop can be as thin as an ion gyro-radius, because cross-field transport is inhibited in a low- β plasma. The instrument-limited fine structure appears as shown in Fig. 1.18: an apparently compact loop seen at low resolution may reveal a bundle of fine threads at high resolution.

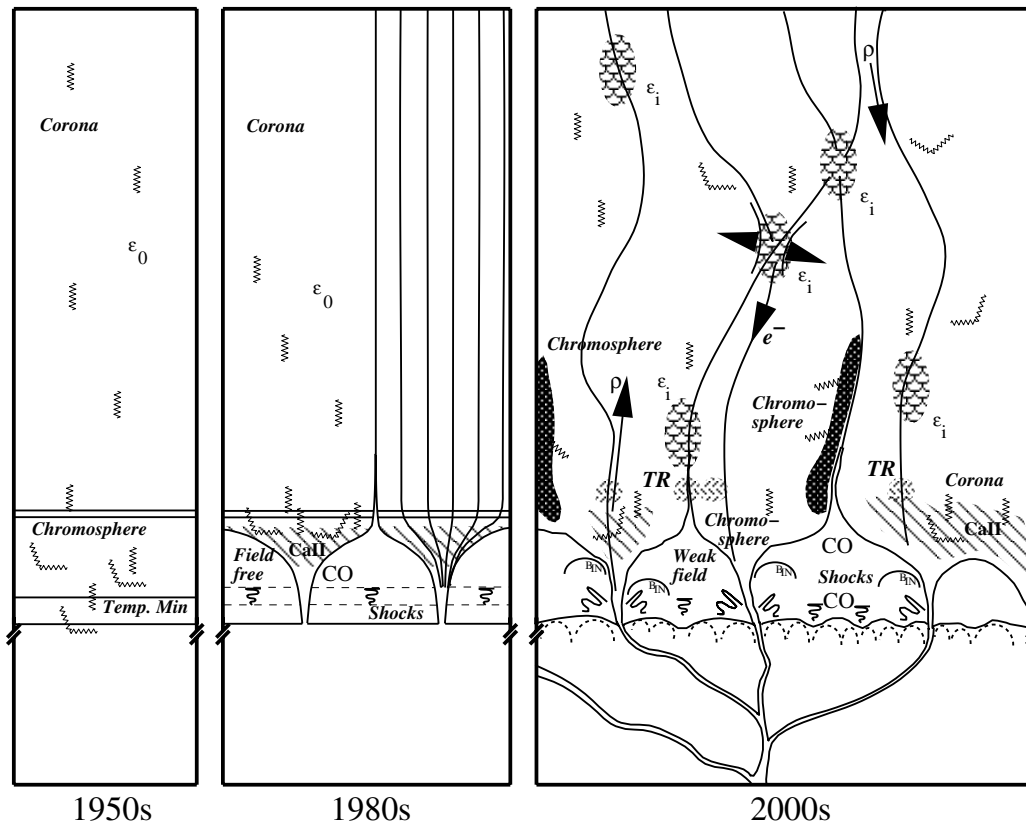


Figure 1.17: Cartoon of geometric concepts of the solar corona: gravitationally stratified layers in the 1950s (*left*), vertical fluxtubes with chromospheric canopies in the 1980s (*middle*), and a fully inhomogeneous mixing of photospheric, chromospheric, and coronal zones by dynamic processes such as heated upflows, cooling downflows, intermittent heating (ϵ), nonthermal electron beams (e), field line motions and reconnections, emission from hot plasma, absorption and scattering in cool plasma, acoustic waves, and shocks (*right*) (Schrijver, 2001b).

Given these geometrical concepts, we can partition the solar corona into open-field and closed-field regions, as shown in Fig. 1.14. Because the 3D magnetic field is space-filling, every location can be associated with a particular magnetic field line. Depending on the desired spatial resolution of a geometric model, each domain of the corona can further be subdivided into magnetic fluxtubes with a certain cross-sectional area, each one representing an isolated “mini-atmosphere”, having its own gravitational stratification and hydrostatic pressure balance, constrained by different densities and temperatures at the lower boundary. This breakdown of the inhomogeneous atmosphere into separate fluxtubes simplifies the magneto-hydrostatics into 1D transport processes. Measurements of the flux in EUV or soft X-rays, which is an optically thin emission, however, involves various contributions from different fluxtubes along a line-of-sight, requiring the knowledge of the statistical distribution of fluxtubes. EUV and soft X-ray data can therefore only be modeled in terms of *multi-fluxtube* or *multi-temperature* concepts.

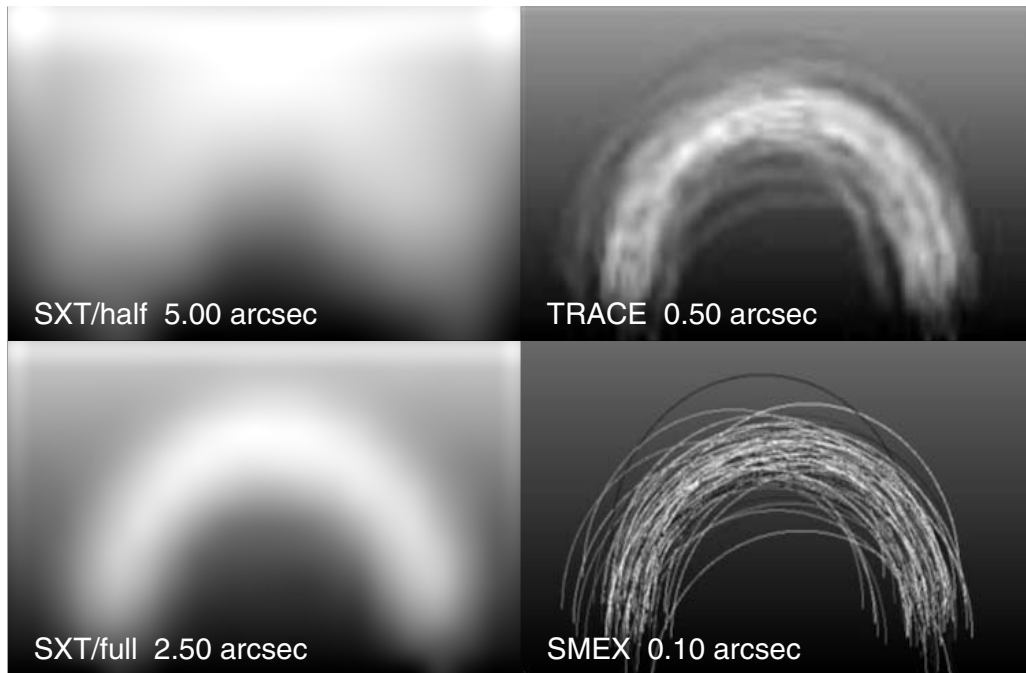


Figure 1.18: Concept of multi-thread loops, which exhibit more or less fine structure depending on the angular resolution of the observing instrument. Four different representations of the same bundle of bright magnetic field lines are shown, observed with angular resolutions of $5''$ and $2.5''$ (*SXT/Yohkoh*, *EIT/SoHO*), $0.5''$ (*TRACE*), and with $0.1''$ (a proposed future *SMEX* mission).

1.6 Density Structure of the Solar Corona

The particle density in the corona, and even in the chromosphere, is much lower than the best vacuum that can be generated in any laboratory on Earth. Electron densities in the solar corona range from $\approx 10^6 \text{ cm}^{-3}$ in the upper corona (at a height of one solar radius) to $\approx 10^9 \text{ cm}^{-3}$ at the base in quiet regions, and can increase up to $\approx 10^{11} \text{ cm}^{-3}$ in flare loops. The transition region at the base of the corona demarcates an abrupt boundary where the chromospheric density increases several orders of magnitude higher than coronal values (Fig. 1.19) and the temperature drops below 11,000 K, the ionization temperature of hydrogen. The chromospheric plasma is therefore only partially ionized, while the coronal plasma is fully ionized. Chromospheric density models have been calculated in great detail, based on ion abundance measurements from a large number of EUV lines, constrained by hydrostatic equilibrium, radiation transfer (Vernazza et al. 1973, 1976, 1981), and ambipolar diffusion (Fontenla et al. 1990, 1991).

The density models shown in Fig. 1.19 represent an average 1D model for a gravitationally stratified vertical fluxtube. There are, however, a lot of dynamic processes that heat up the chromospheric plasma, which is then driven by the overpressure upward into the corona, producing over-dense structures with densities in excess of the ambient quiet corona. In order to give a feeling for the resulting density variations in

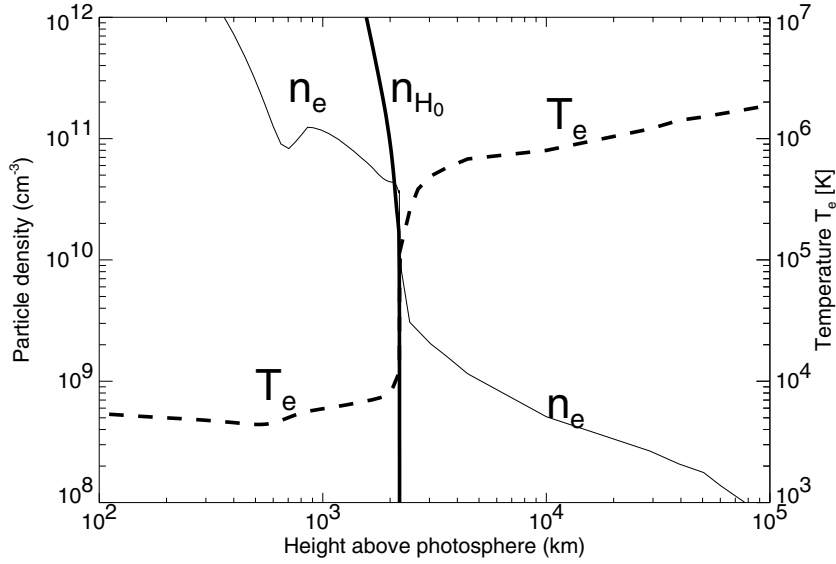


Figure 1.19: Electron density and temperature model of the chromosphere (Fontenla et al. 1990; Model FAL-C) and lower corona (Gabriel, 1976). The plasma becomes fully ionized at the sharp transition from chromospheric to coronal temperatures. In the chromosphere, the plasma is only partially ionized: n_e indicates the electron density, n_{H_0} the neutral hydrogen density.

the highly inhomogeneous corona we show a compilation of density measurements in Fig. 1.20, sampled in coronal holes, quiet Sun regions, coronal streamers, and active regions. At the base of the corona, say at a nominal height of ≈ 2500 km above the photosphere, the density is lowest in coronal holes, typically around $\approx (0.5 - 1.0) \times 10^8$ cm^{-3} . In quiet Sun regions the base density is generally higher (i.e., $\approx (1 - 2) \times 10^8$ cm^{-3}). At the base of coronal streamers, the density climbs to $\approx (3 - 5) \times 10^8$ cm^{-3} , and in active regions it is highest at $\approx 2 \times 10^8 - 2 \times 10^9$ cm^{-3} . In the upper corona, say at heights larger than 1 solar radius, the density drops below $10^6 - 10^7$ cm^{-3} .

Coronal densities were first measured from white-light (polarized brightness) data using a Van de Hulst (1950a,b) inversion, assuming that the polarized brightness of white light is produced by Thomson scattering and is proportional to the line-of-sight integrated coronal electron density. Another ground-based method uses the frequency of radio bursts that propagate through the corona, assuming that their emission frequency corresponds to the fundamental or harmonic plasma frequency, which is a direct function of the electron density. During the last several decades, space-borne observations in EUV and soft X-rays provided another method, based on the emission measure, which is proportional to the squared density integrated along the column depth, for optically thin radiation. This latter method can be performed in different spectral lines so that the densities can be measured independently for plasmas with different temperatures. However, since every instrument has a limited spatial resolution that may not adequately resolve individual plasma structures, the inferred densities place only lower limits on the effective densities. Absolute densities can be measured from some density sensitive lines in the $1 - 20$ \AA range, at relatively high densities of $n_e \gtrsim 10^{12}$ cm^{-3} (e.g., the Fe XXI and Fe XXII lines; Phillips et al. 1996).

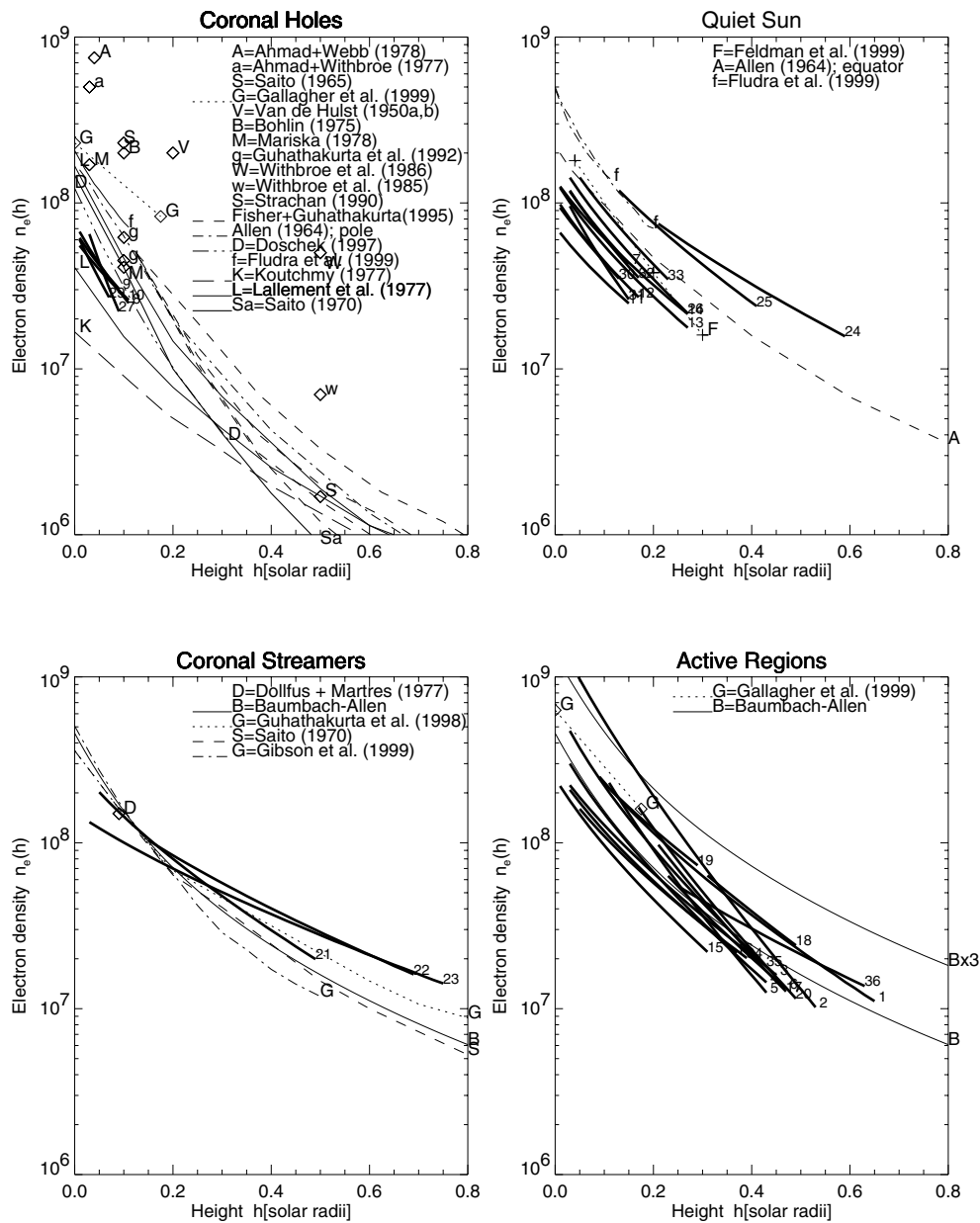


Figure 1.20: Compilation of electron density measurements in the height range of $0.003 < h < 0.8$ solar radii or $2500 < h < 560,000$ km: in coronal holes (top left), quiet Sun regions (top right), coronal streamers (bottom left), and in active regions (bottom right). Note that the electron density at any given height varies 1–2 orders of magnitude over the entire corona. The numbered curves (with thick linestyle) represent soft X-ray measurements from Aschwanden & Acton (2001).

From white-light observations during solar eclipses, the corona was characterized by three components: (1) the K-corona, made of partially polarized continuum emission from photospheric light scattered at free electrons (dominating at $h \lesssim 0.3$ solar radius);

(2) the L-corona, consisting of spectral line emission from highly ionized atoms (dominating at $h \lesssim 0.5$ solar radius); and (3) the F corona, which presents absorption lines of the photospheric Fraunhofer spectrum caused by diffraction from interplanetary dust (dominating at $h \gtrsim 0.5$ solar radius). The line-of-sight integrated density profiles of these three components can be approximated by a powerlaw function, each leading to an average density profile known as the *Baumbach–Allen formula* (e.g., Cox, 2000),

$$n_e(R) = 10^8 \left[2.99 \left(\frac{R}{R_\odot} \right)^{-16} + 1.55 \left(\frac{R}{R_\odot} \right)^{-6} + 0.036 \left(\frac{R}{R_\odot} \right)^{-1.5} \right] \text{ cm}^{-3} \quad (1.6.1)$$

parametrized by the distance $R = R_\odot + h$ from the Sun center. Density measurements from eclipse observations can be performed out to distances of a few solar radii. Further out in interplanetary space, heliospheric densities can be measured by scintillations of radio sources (Erickson, 1964),

$$n_e(R) \approx 7.2 \times 10^5 \left(\frac{R}{R_\odot} \right)^{-2} \text{ cm}^{-3}, \quad R \gg R_\odot \quad (1.6.2)$$

or from the plasma frequency or interplanetary radio bursts.

1.7 Temperature Structure of the Solar Corona

The temperature of the solar corona was first asserted only 60 years ago. In 1940, Bengt Edlén analyzed spectral lines following the diagrams of Walter Grotrian and established that coronal emission arises from highly ionized elements, at temperatures of $\gtrsim 1$ MK (1 MegaKelvin = 1,000,000 Kelvin). The physical understanding of this high temperature in the solar corona is still a fundamental problem in astrophysics, because it seems to violate the second thermodynamic law, given the much cooler photospheric boundary, which has an average temperature of $T = 5785$ K (and drops to $T \approx 4500$ K in sunspots). The rapid temperature rise from the chromosphere to the corona is shown in Fig. 1.19 (dashed curve). Further out in the heliosphere, the coronal temperature drops slowly to a value of $T \approx 10^5$ K at 1 AU.

The temperature structure of the solar corona is far from homogeneous. The optically thin emission from the corona in soft X-rays (Fig. 1.8) or in EUV implies over-dense structures that are filled with heated plasma. The only available reservoir is the chromosphere, which apparently needs to be heated at many locations, to supply coronal loops with hot upflowing plasma. Because the thermal pressure is generally smaller than the magnetic pressure (plasma- β parameter < 1), plasma transport occurs only in one dimension along the magnetic field lines, while cross-field diffusion is strongly inhibited. This has the consequence that every coronal loop represents a thermally isolated system, having only the tiny chromospheric footpoints as valves for rapid heat and mass exchange. Because the heating of the footpoints of coronal loops seems to be spatially and temporally intermittent, every loop ends up with a different energy input and settles into a different temperature, when a quasi-steady heating rate is obtained. Consequently, we expect that the corona is made up of many filled loops with different

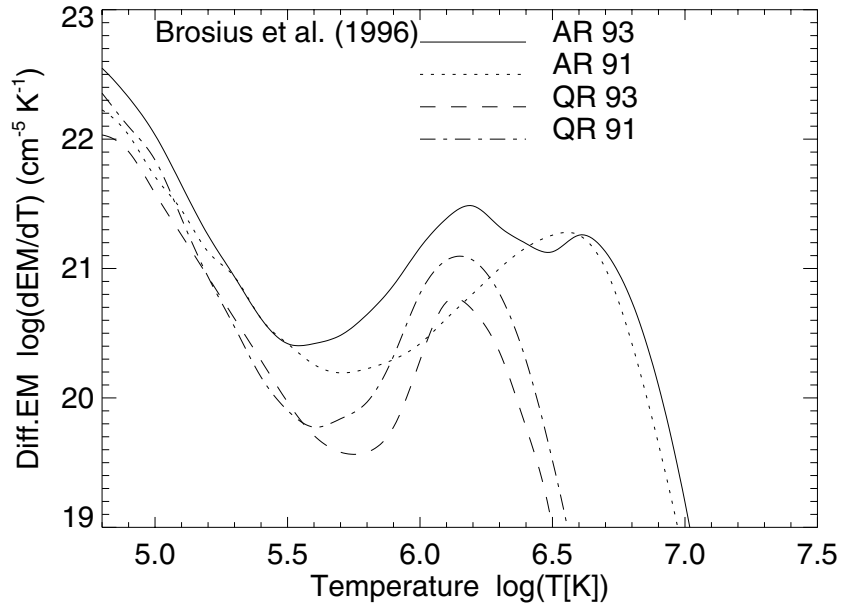


Figure 1.21: Differential emission measure distribution $dEM(T)/dT$ of two active regions (AR 93, AR 91) and two quiet Sun regions (QR 93, QR 91) measured by Brosius et al. (1996) with *SERTS* data.

temperatures, the cooler ones visible in EUV and the hotter ones shining in soft X-rays. Such a multi-temperature picture of the solar corona is shown in Plate 1, composed of three images taken with different temperature filters with *EIT/SoHO*: a blue image at 1.0 MK (171 Å), a green image at 1.5 MK (195 Å), and a red image at 2.0 MK (284 Å). Following the color coding, one can clearly see in Plate 1 that the northern coronal hole contains the coolest regions and that the temperature seems to increase with altitude above the limb. In §3 we will learn that this apparent temperature increase does not reflect a positive temperature gradient with height along individual field lines, but merely results from the relative density weighting of cool and hot (hydrostatic) temperature scale heights. Another effect that can be seen in Plate 1 is the law of additive color mixing according to Isaac Newton: If blue, green, and red are mixed with equal weighting, white results. The white color-coding in active regions seen in Plate 1 can therefore be taken as evidence that active regions contain comparable temperature contributions from 1.0, 1.5, and 2.0 MK temperature loops.

The multi-temperature distribution of the corona can quantitatively be expressed by the so-called *differential emission measure distribution* $dEM(T)/dT$, which is a measure of the squared density $n_e(T)$ integrated over the column depth along the line-of-sight for any given temperature,

$$\frac{dEM(T)}{dT} dT = \int n_e^2(T, z) dz . \quad (1.7.1)$$

This quantity can be measured with a broad range of EUV and soft X-ray lines at any location (or line-of-sight) on the Sun. Such differential emission measure distributions obtained from 4 different locations are shown in Fig. 1.21, two in quiet Sun regions

and two in active regions, obtained from He II, C IV, Mg V, Ca VII, Mg VI, Mg VIII, Fe X, Si IX, Fe XI, Al X, Si XI, Fe XV, Fe XVI, and Ni XVIII lines with the *Solar EUV Research Telescope and Spectrograph (SERTS)* on sounding rocket flights during 1991 and 1993 (Brosius et al. 1996). The set of EUV emission lines used is sensitive in the temperature range of $\log(T) = 4.8 - 6.5$ ($T = 63,000 \text{ K} - 3.2 \text{ MK}$). The DEM distribution in Fig. 1.21 clearly shows a temperature peak around $\log(T) = 6.0 - 6.3$ for the quiet Sun regions, which corresponds to the $T = 1 - 2 \text{ MK}$ range, which is coincident with the blue-red color range in Plate 1. In active regions, the DEM distributions in Fig. 1.21 show a comparable amount of emission measure in the temperature range of $\log(T) = 6.3 - 6.8$, which corresponds to temperatures of $T = 2.0 - 6.3 \text{ MK}$.

This coarse temperature characterization of the corona already shows an interesting trend. Open-field regions, such as coronal holes (Fig. 1.14), have the coolest temperatures of $T \lesssim 1 \text{ MK}$; closed-field regions, such as the quiet Sun, have intermediate temperatures of $T \approx 1 - 2 \text{ MK}$; while active regions exhibit the hottest temperatures of $T \approx 2 - 6 \text{ MK}$. Open-field regions seem to be cooler because plasma transport is very efficient, while closed-field regions seem to be hotter because the heated plasma is trapped and cannot easily flow away. The temperature difference between quiet Sun and active regions is a consequence of different magnetic flux emergence rates, heating rates, conductive loss rates, radiative loss rates, and solar wind loss rates.

1.8 Plasma- β Parameter of the Solar Corona

The magnetic field B exerts a Lorentz force on the charged particles of the coronal plasma, consisting of electrons and ions, guiding them in a spiraling gyromotion along the magnetic field lines. Only when the kinetic energy exceeds the magnetic energy (i.e., at high temperatures and low magnetic fields), can particles escape their gyro-orbits and diffuse across the magnetic field. The critical parameter between these two confinement regimes is the plasma- β parameter, defined as the ratio of the thermal plasma pressure p_{th} to the magnetic pressure p_m ,

$$\beta = \frac{p_{th}}{p_m} = \frac{2\xi n_e k_B T_e}{B^2/8\pi} \approx 0.07 \xi n_9 T_6 / B_1^2, \quad (1.8.1)$$

where $\xi = 1$ is the ionization fraction for the corona (and $\xi = 0.5$ in the photosphere), $k_B = 1.38 \times 10^{-16} \text{ erg K}^{-1}$ the Boltzmann constant, $B_1 = B/10 \text{ G}$ the magnetic field strength, $n_9 = n_e/10^9 \text{ cm}^{-3}$ the electron density, and $T_6 = T/10^6 \text{ K}$ the electron temperature. In Table 1.1 we list some typical parameters for the chromosphere, and cool, hot, and outer parts of the corona.

We see that most parts of the corona have a plasma- β parameter of $\beta < 1$, but are sandwiched between the higher values $\beta > 1$ in the chromosphere and outer corona. Therefore, most parts of the corona are magnetically confined. However, hot regions with low magnetic fields (e.g., in the magnetic cusps above streamers), can easily have values of $\beta > 1$, so that plasma can leak out across the cusped magnetic field lines. Most magnetic field extrapolation codes do not or cannot take into account the full range of β and essentially assume $\beta \ll 1$. The inference of the plasma- β parameter in

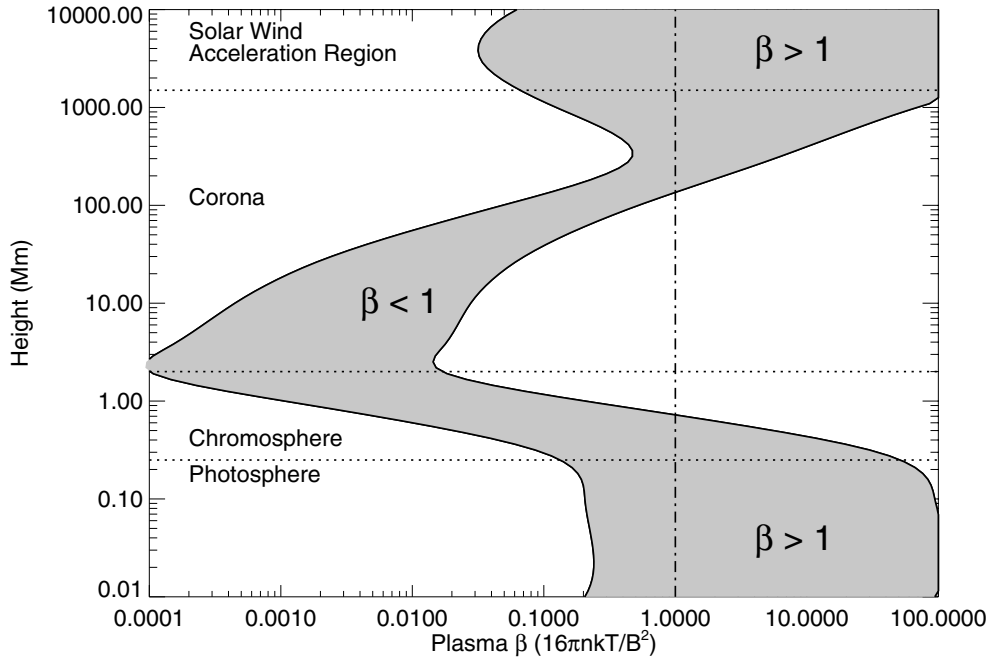


Figure 1.22: Plasma β in the solar atmosphere for two assumed field strengths, 100 G and 2500 G. In the inner corona ($R \lesssim 0.2R_{\odot}$), magnetic pressure generally dominates static gas pressure. As with all plots of physical quantities against height, a broad spatial and temporal average is implied (Gary, 2001).

Table 1.1: The plasma- β parameter in the solar atmosphere.

Parameter	Photosphere	Cool corona	Hot corona	Outer corona
Electron density n_e (cm^{-3})	2×10^{17}	1×10^9	1×10^9	1×10^7
Temperature T (K)	5×10^3	1×10^6	3×10^6	1×10^6
Pressure p (dyne cm^{-2})	1.4×10^5	0.3	0.9	0.02
Magnetic field B (G)	500	10	10	0.1
Plasma- β parameter	14	0.07	0.2	7

different locations of the solar corona thus strongly depends on the employed magnetic field model, in particular because the magnetic field strength B is the least known physical parameter in the corona, while the density n_e and temperature T_e can readily be measured in EUV and soft X-rays for structures with good contrast to the coronal background. A comprehensive model of the plasma- β parameter has been built by Gary (2001), using a large number of physical parameters quoted in the literature, resulting in a well-constrained range of β -values for any given height, $\beta(h)$, shown as a grey zone in Fig. 1.22. One conclusion of Gary (2001) is that even in coronal heights of $h \gtrsim 0.2R_{\odot}$ high β -values above unity can occur, which might be responsible for the dynamics of cusp regions (Fig. 1.23) or overpressure near the apices of large loops seen with *TRACE*.

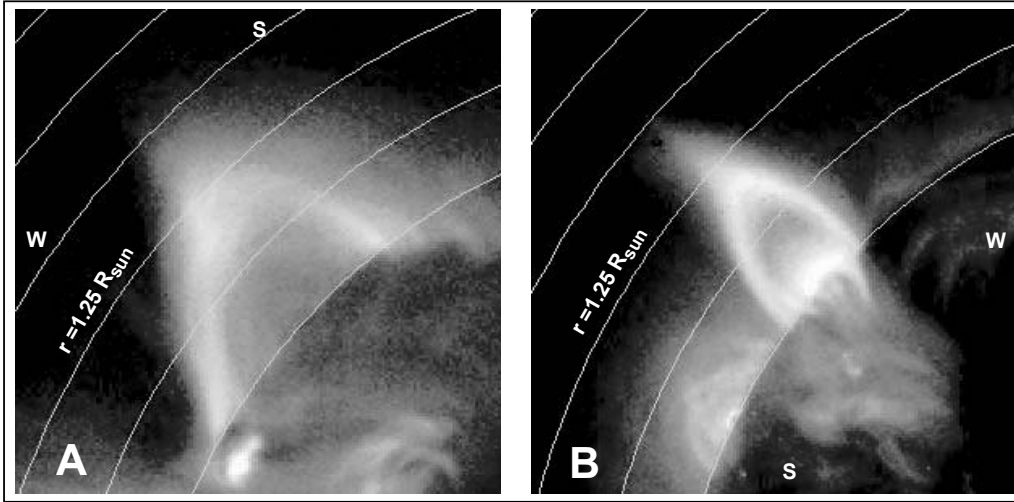


Figure 1.23: Two cusped loops observed by *SXT/Yohkoh* are shown at the west limb on 1992 January 24 (rotated, A) and the east limb on 1999 March 18 (B). The cusps are at a height of $r = 0.23R_{\odot}$ and $r = 0.25R_{\odot}$. The pressure and inertial forces of the solar wind dominate over the magnetic forces at the cusp and distend the field outwards. This implies $\beta \gtrsim 1$ at these heights (Gary, 2001).

1.9 Chemical Composition of the Solar Corona

Atomic spectroscopy that led to a first quantitative analysis of the chemical composition of the photosphere was pioneered by Henry Norris Russell in 1929. The chemical composition of the Sun has been measured most accurately in the photosphere, where line emission is brightest, while measurements of elemental abundances in the corona are much less sensitive, due to the corona being many orders of magnitude fainter. The chemical composition in the photosphere and corona are largely similar for most of the elements, and are also consistent with cosmic abundances, as they have been measured from chemical analyses of meteorites. The most recent comparison of photospheric and meteorite elemental abundances can be found, for example in Grevesse & Sauval (2001), where significant differences are listed only for the element of lithium. From the same source we list elemental abundances measured in the photosphere and corona (Table 1.2), and show the logarithmic abundances in Fig. 1.24. It can be seen that coronal elements have only currently been detected up to an atomic number of $Z \leq 30$, essentially elements down to a fraction of $\gtrsim 10^{-6}$ of the hydrogen abundance, while the sensitivity limit in the photosphere reaches $\approx 10^{-12}$.

There are a few special elements. The abundance of helium cannot be measured in the photosphere, simply because no helium line (neutral or single-ionized species) falls within the wavelength range covered by the photospheric spectrum, in the (photospheric) temperature range around 5000 K. Also for the same reason, the noble gases neon and argon cannot be measured in the photosphere. Theoretical stellar models that fit the observed age, mass, diameter, and luminosity of the Sun yield a helium abundance of $A_{He}/A_H = 9.8 \pm 0.4\%$ for the protosolar cloud. A slightly lower value is

Table 1.2: Elemental abundances in the solar photosphere and corona.

Element	Abundance ¹ Photosphere	Abundance ¹ Corona	FIP [eV]	Element	Abundance ¹ Photosphere
1 H	12.00	12.00	13.6	42 Mo	1.92 ± 0.05
2 He	-	10.93 ± 0.004	24.6	44 Ru	1.84 ± 0.07
3 Li	1.10 ± 0.10 ²	-	5.4	45 Rh	1.12 ± 0.12
4 Be	1.40 ± 0.09	-	9.3	46 Pd	1.69 ± 0.04
5 B	(2.55 ± 0.30)	-	8.3	47 Ag	(0.94 ± 0.25)
6 C	8.52 ± 0.06	8.5	11.3	48 Cd	1.77 ± 0.11
7 N	7.92 ± 0.06	7.9	14.5	49 In	(1.66 ± 0.15)
8 O	8.83 ± 0.06 ²	8.8	13.6	50 Sn	2.0 ± 0.3
9 F	4.56 ± 0.30 ²	-	17.4	51 Sb	1.0 ± 0.3
10 Ne	-	8.08 ± 0.06	21.6	52 Te	-
11 Na	6.33 ± 0.03	6.3 ³	5.2	53 I	-
12 Mg	7.58 ± 0.05	7.6 ³	7.6	54 Xe	-
13 Al	6.47 ± 0.07	6.4 ³	6.0	55 Cs	-
14 Si	7.55 ± 0.05	7.6 ³	8.1	56 Ba	2.13 ± 0.05
15 P	5.45 ± 0.04	5.5	10.5	57 La	1.17 ± 0.07
16 S	7.33 ± 0.11	7.2	10.3	58 Ce	1.58 ± 0.09
17 Cl	5.50 ± 0.30 ²	5.8	13.0	59 Pr	0.71 ± 0.08
18 Ar	-	6.40 ± 0.06 ³	15.8	60 Nd	1.50 ± 0.06
19 K	5.12 ± 0.13	-	4.3	62 Sm	1.01 ± 0.06
20 Ca	6.36 ± 0.02	6.3 ³	6.1	63 Eu	0.51 ± 0.08
21 Sc	3.17 ± 0.10	-		64 Gd	1.12 ± 0.04
22 Ti	5.02 ± 0.06	-		65 Tb	(-0.1 ± 0.3)
23 V	4.00 ± 0.02	-		66 Dy	1.14 ± 0.08
24 Cr	5.67 ± 0.03	-	6.8	67 Ho	(0.26 ± 0.16)
25 Mn	5.39 ± 0.03	-	7.4	68 Er	0.93 ± 0.06
26 Fe	7.50 ± 0.05	7.6 ³	7.9	69 Tm	(0.00 ± 0.15)
27 Co	4.92 ± 0.04	5.0		70 Yb	1.08 ± 0.15
28 Ni	6.25 ± 0.04	6.3 ³	7.6	71 Lu	0.06 ± 0.10
29 Cu	4.21 ± 0.04	4.1		72 Hf	0.88 ± 0.08
30 Zn	4.60 ± 0.08	4.4		73 Ta	-
31 Ga	2.88 ± 0.10 ²	-	6.0	74 W	(1.11 ± 0.15)
32 Ge	3.41 ± 0.14 ²	-		75 Re	-
33 As	-	-		76 Os	1.45 ± 0.10
34 Se	-	-		77 Ir	1.35 ± 0.10
35 Br	-	-		78 Pt	1.8 ± 0.3
36 Kr	-	-	14.0	79 Au	(1.01 ± 0.15)
37 Rb	2.60 ± 0.15 ²	-	4.2	80 Hg	-
38 Sb	2.97 ± 0.07	-		81 Tl	(0.9 ± 0.2)
39 Y	2.24 ± 0.03	-		82 Pb	1.95 ± 0.08
40 Zr	2.60 ± 0.02	-		83 Bi	-
41 Nb	1.42 ± 0.06	-		90 Th	-
				92 U	< -0.47)

¹) abundances are given on a logarithmic scale, $12.0 +^{10} \log(A/A_H)$ ²) derived in addition or only from sunspots³) abundance could be a factor of ≈ 3 times higher in corona and solar wind (low-FIP)

(...) Values between parentheses are less accurate

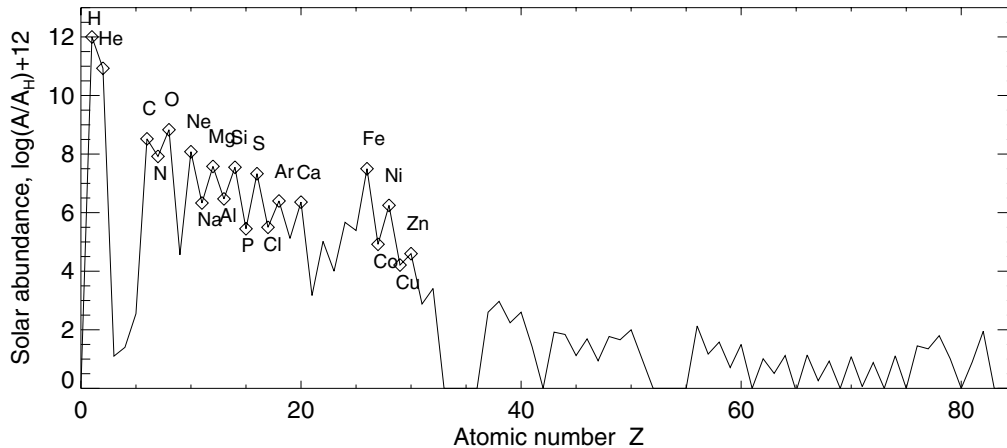


Figure 1.24: Logarithmic distribution of the abundance of the elements relative to hydrogen, normalized to $12 + \log(A/A_H[Z = 1])$, as a function of the atomic number, Z . Elements that have been detected in the corona are labeled.

obtained from inversion of helioseismic data. Other exceptions are the light elements of lithium, beryllium, and boron, which have a strikingly low abundance as a consequence of their low *nuclear binding energy*, so that these nuclei are destroyed by proton collisions at solar temperatures of a few million Kelvins.

Since the solar corona is a highly dynamic and inhomogeneous place, subtle variations in the chemical composition have been observed in various coronal structures. A fractionation seems to occur in the lower chromospheric layers, where elements with a low *first ionization potential (FIP)* (≤ 10 keV) show abundances that are locally and temporarily larger than in the photosphere. Such a FIP fractionation effect can change the relative abundances typically by a factor of ≈ 3 (e.g., Na, Mg, Al, Si, Ca, Ni), or up to a factor of 10 for iron (Fe), between the chromosphere and the solar wind. Unfortunately the relative abundances cannot directly be measured with respect to hydrogen, because hydrogen is completely ionized in the corona, so that it has no emission lines that can be used for absolute abundance determinations. Instead, only relative abundances of “heavy” elements (metals) can be measured, so that there is an ambiguity whether the FIP fractionation effect causes an enhancement of low-FIP elements into the corona, or a depletion of high-FIP elements out of the corona (to the chromosphere).

1.10 Radiation Spectrum of the Solar Corona

The atmosphere of our planet Earth filters out emission from the Sun and stars in many wavelengths, except for two spectral windows at optical and radio wavelengths. The major progress in solar physics achieved over the last decade thus involves a number of space missions, floating aloft our absorbing atmosphere. These space missions provide us unprecedented information over the entire wavelength spectrum, covering gamma-rays, hard X-rays, soft X-rays, X-ray ultraviolet (XUV), extreme ultraviolet (EUV), and ultraviolet (UV). It has opened our eyes about the physical processes that govern solar and stellar atmospheres that we could not anticipate without space data. An overview

of the solar radiation spectrum is shown in Fig. 1.25, covering a wavelength range over 14 orders of magnitude.

The physical units of the spectrum are generally quantified in terms of the wavelength λ (bottom axis of Fig. 1.25), having units of meters (m) in the SI system or centimeters (cm) in the cgs system. However, astronomers often prefer Ångström (Å) units, defined by,

$$1 \text{ \AA} = 10^{-8} \text{ cm} = 10^{-10} \text{ m} . \quad (1.10.1)$$

In the radio domain, the frequency unit ν is used (top axis in Fig. 1.25), which has the unit (Hz) or (s^{-1}) in both the SI or cgs system and can be calculated from the basic dispersion relation of electromagnetic waves in a vacuum,

$$\nu = \frac{c}{\lambda} , \quad (1.10.2)$$

with $c = 2.9979 \times 10^{10} \text{ cm s}^{-1}$ being the speed of light. For relativistic particles, as we observe in hard X-rays and gamma-rays in the solar corona and chromosphere, a practical unit is eV. An electron-Volt (1 eV) is defined by the energy gained by an electron (e) if it is accelerated by a potential difference of 1 Volt (V), which is in SI and cgs units,

$$1 \text{ eV} = 1.60 \times 10^{-19} \text{ C} \times 1 \text{ V} = 1.60 \times 10^{-19} \text{ J} = 1.60 \times 10^{-12} \text{ erg} . \quad (1.10.3)$$

Equating the particle energy ε with the photon quantum energy $\epsilon = h\nu$, we then have (with Eq.1.10.2) a relation to the wavelength λ ,

$$\epsilon = h\nu = h\frac{c}{\lambda} = 12.4 \left(\frac{1 \text{ \AA}}{\lambda} \right) \text{ keV} . \quad (1.10.4)$$

For thermal plasmas, which are observed in the solar corona in EUV, XUV, and in soft X-rays, it is customary to associate a temperature T with a wavelength λ , using the definition of the quantum energy of a photon (and the dispersion relation 1.10.2),

$$\varepsilon_{th} = k_B T = \epsilon = h\nu = h\frac{c}{\lambda} . \quad (1.10.5)$$

This yields (with the Boltzmann constant $k_B = 1.38 \times 10^{-16} \text{ erg K}^{-1}$ and the Planck constant $h = 6.63 \times 10^{-27} \text{ erg s}$) the conversion formula,

$$T = \frac{hc}{k_B \lambda} = 1.44 \left(\frac{1 \text{ cm}}{\lambda} \right) \text{ K} . \quad (1.10.6)$$

With these relations we can conveniently convert any physical unit used in the context of a wavelength spectrum. The solar irradiance spectrum from gamma-rays to radio waves is shown in Fig.1.25, given in units of energy per time, area, and wavelength ($\text{erg s}^{-1} \text{ cm}^{-2} \mu\text{m}^{-1}$).

Let us tour quickly from the shortest to the longest wavelength regime, summarizing in each one the essential physical emission processes that can be detected with space-borne instruments and ground-based telescopes.

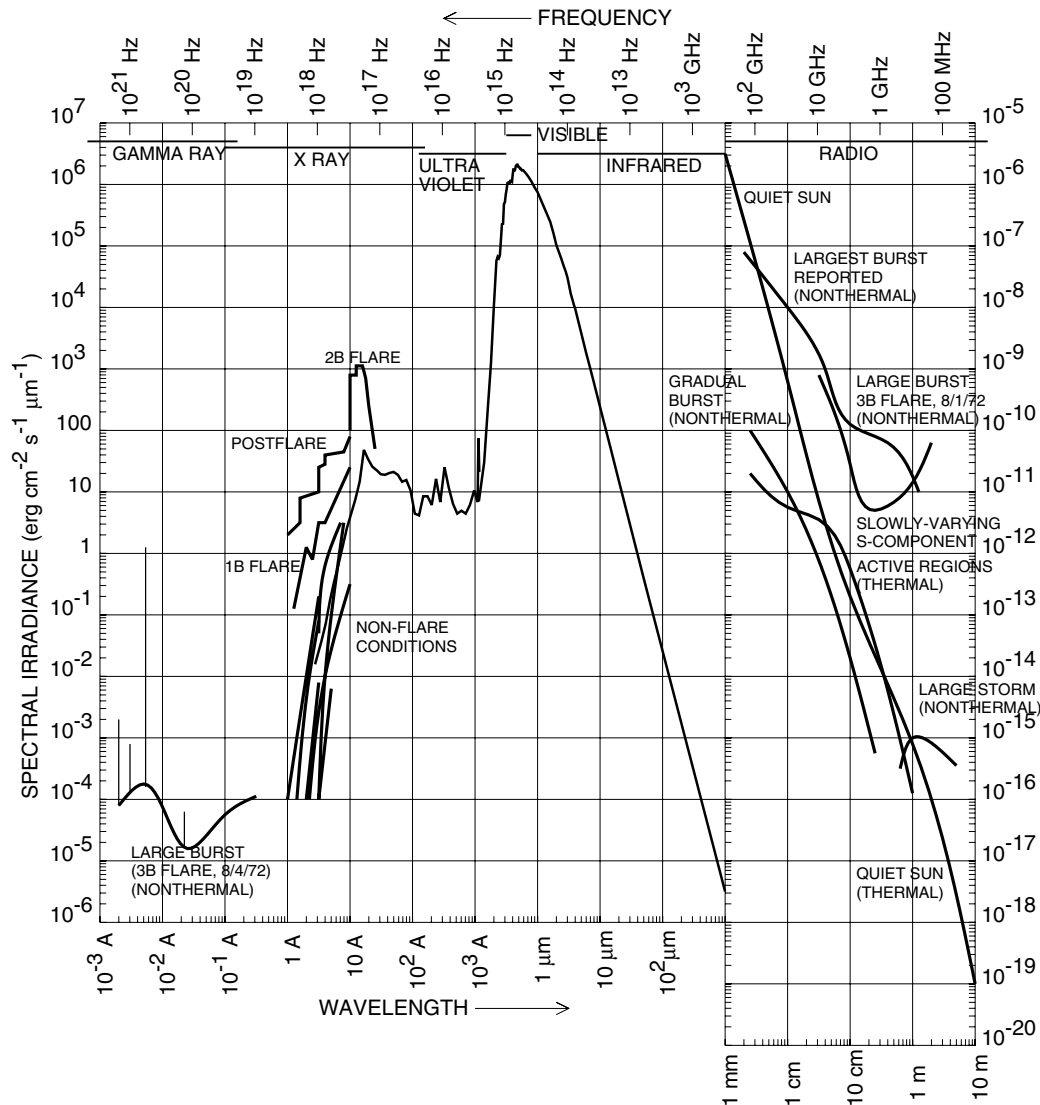


Figure 1.25: The solar irradiance spectrum from gamma-rays to radio waves. The spectrum is shifted by 12 orders of magnitude in the vertical axis at $\lambda = 1$ mm to accommodate for the large dynamic range in spectral irradiance (after Zombeck, 1990 and Foukal, 1990).

The shortest wavelength regime, which is emitted during only the most energetic processes in large flares, is the *gamma-ray* (γ -ray) regime, in a wavelength range of $\lambda \approx 10^{-3} - 10^{-1}$ Å, which corresponds to energies of $\epsilon \approx 100$ keV–10 MeV. Obviously, such high-energy radiation is only emitted from the Sun when particles are accelerated in flares to sufficiently high energies, so that they can interact with atomic nuclei. Solar gamma-ray emission is produced when particles, accelerated to high energies in the collisionless corona, precipitate to the chromosphere, where a number of nuclear processes produce gamma-rays (e.g., continuum emission by primary electron bremsstrahlung, nuclear de-excitation lines, neutron capture lines, positron annihilation radiation, or pion decay radiation).

The next wavelength regime is the *hard X-rays* regime, corresponding to wavelengths of $\lambda \approx 0.1 - 1 \text{ \AA}$ or energies of $\epsilon \approx 10 - 100 \text{ keV}$. This energy range corresponds to mild-to-medium relativistic electrons (with a rest mass of $m_e c^2 = 511 \text{ keV}$ and a relativistic speed of $\beta = v/c \approx 0.2 - 0.5$), and thus requires electrons that are accelerated in a collisionless plasma in the corona. When these nonthermal electrons enter the high-density transition region and chromosphere, they lose their energy by collisions and emit electron (thick-target) bremsstrahlung, which is seen at hard X-ray wavelengths.

The next wavelength regime is called *soft X-rays*, at wavelengths of $\lambda \approx 1 - 100 \text{ \AA}$. This soft X-ray wavelength range corresponds to thermal energies of $\epsilon_{th} \approx 0.1 - 10 \text{ keV}$ and plasma temperatures of $T \approx 1.5 - 150 \text{ MK}$. Such plasma temperatures are found in active regions ($T \approx 1.5 - 10 \text{ MK}$) and in flare loops ($T \approx 10 - 40 \text{ MK}$). This entire wavelength regime is well observed with the *Soft X-Ray Telescope (SXT)* on board *Yohkoh*. The longer wavelength decade at $\lambda \approx 10 - 100 \text{ \AA}$ is also called *X-ray ultraviolet (XUV)*. Soft X-rays are produced by free-free emission of electrons that are scattered off highly-ionized ions in the solar corona.

The next wavelength decade is *extreme ultraviolet (EUV)*, covering wavelengths of $\lambda \approx 100 - 1000 \text{ \AA}$ or temperatures of $T \approx 0.15 - 1.5 \text{ MK}$. As it can be seen from the differential emission measure distribution (Fig.1.21), most of the plasma in the quiet Sun has temperatures around $T \approx 1 - 3 \text{ MK}$, and thus the quiet Sun is best probed with EUV lines. Both EUV imagers, the *EIT/SoHO* and *TRACE*, have their primary passbands in this wavelength regime, i.e., 171 \AA ($T \approx 1.0 \text{ MK}$), 195 \AA ($T \approx 1.5 \text{ MK}$), and 284 \AA ($T \approx 2.0 \text{ MK}$) wavebands. EUV emission is also produced by free-free emission like for soft X-rays, but by scattering off ions with lower temperatures, Fe IX to Fe XV.

The peak of the solar irradiance spectrum is, of course, in the optical wavelength regime of $\lambda \approx 3000 - 7000 \text{ \AA}$ that is visible to the eye. It is probably an evolutionary adaption process that our eyes developed the highest sensitivity where our Sun provides our life-supporting daylight. Optical emission from the Sun originates mostly from continuum emission in the photosphere, so that we do not gain much information from the corona in visible light. It is only during total solar eclipses, when the bright light from the solar disk is occulted by the moon, that faint scattered light reveals us some structures from the tenuous corona.

The next three decades of the wavelength spectrum is called *infrared*, extending over $\lambda \approx 1 \text{ \mu m} - 1 \text{ mm}$. Infrared emission does not contain many lines, the most prominent one longward of 1 \mu m is the He $10,830 \text{ \AA}$ line. Most of the infrared is dominated by low-excitation species: neutral atoms and molecules (e.g., carbon monoxide, hydroxyl, water vapor). Infrared emission is thus only produced in quiescent gas not strongly heated, conditions that can be found in supergranulation cell interiors and in sunspot umbrae.

Finally, the longest wavelength regime is occupied by *radio wavelengths*, from $\lambda \approx 1 \text{ mm}$ to 10 m , corresponding to frequencies of $\nu \approx 300 \text{ GHz}$ to 30 MHz . In radio there are a variety of emission mechanisms that radiate at characteristic frequencies: gyrosynchrotron emission produced by high-relativistic electrons during flares (microwaves: dm, cm, mm wavelengths), gyroresonance emission from mildly relativistic electrons in strong magnetic field regions, such as above sunspots (in microwaves),

free-free emission from heated plasma in flares and active regions (dm and cm), plasma emission excited by propagating electron beams (m and dm), and a number of other radiation mechanisms produced by kinetic plasma instabilities. The reason why solar radio emission is so multi-faceted is because the gyrofrequency of coronal magnetic fields as well as the plasma frequency of coronal densities coincide with the radio wavelength range. A large number of ground-based radio telescopes and interferometers have studied this highly interesting spectral window over the last five decades.

1.11 Summary

Observations of the solar corona started with solar eclipses by the moon, which was the only natural means to suppress the strong contrast caused by the six orders of magnitude brighter solar disk in optical wavelengths. Eclipse observations provided the first crude density models of the corona and the discovery of coronal holes. Only the space age, however, allowed a systematic exploration of the other more important wavelength regimes in EUV, soft X-rays, hard X-rays, and gamma-rays. Decade-long spacecraft missions such as SMM, Yohkoh, CGRO, SoHO, and TRACE opened up multi-wavelength observations that were instrumental for diagnostics of coronal plasma physics and high-energy particle physics in flare processes. We note that even the most basic physical properties, such as the density, temperature, and magnetic field structure of solar and stellar coronae are far more complex than any planetary magnetosphere. The coronal magnetic field is driven by an internal dynamo that modulates the surface magnetic field, the solar activity, the coronal brightness, the flare and CME frequency, and the solar wind with an eleven-year cycle, waxing and waning in complexity and non-linear behavior. The density and temperature structure is far from the initially conceived hydrostatic, uniform, and gravitationally stratified atmospheric models, but rather displays a highly dynamic, restless, intricate, and global system that is hidden to us in stellar atmospheres by the concealment of distance. A key parameter that distinguishes the plasma dynamics in the solar corona is the plasma- β parameter, which indicates that the magnetic pressure rather than the thermal pressure governs the coronal plasma dynamics, in contrast to the chromosphere, the solar interior, or the heliosphere. The chemical composition is another peculiarity of the corona, which shows anomalies as a function of the first ionization potential energy (FIP-effect) with respect to the universal chemical composition that is found in the photosphere or in meteorites. The radiation spectrum of the solar corona spans over at least 14 orders of magnitude, from the longest wavelengths in radio over infrared, visible, ultraviolet, soft X-rays, hard X-rays, to gamma-rays, with each wavelength regime revealing different physical processes. Only simultaneous and complementary multi-wavelength observations allow us to establish coherent theoretical models of the fundamental plasma physics processes that operate in the solar corona and in other high-temperature astrophysical plasmas.